이학박사학위논문

Application of super-resolution imaging technique as an analytical tool

분석 기술로 활용한 초고분해능 이미징 기술의 응용 연구

2018 년 8 월

서울대학교 대학원

화학부 물리화학전공

김형준

분석 기술로 활용한 초고분해능 이미징 기술의

응용 연구

Application of super-resolution imaging technique as an analytical tool

지도교수 김 성 근

이 논문을 이학박사학위논문으로 제출함.

2018 년 08 월

서울대학교 대학원
화학부 물리화학전공
김형준

김형준의 이학박사학위논문을 인준함

2018 년 08 월

위 원 장 이 남 기 (인)
부 위 원 장 김 성 근 (인)
위 원 서 정 쌍 (인)
위 원 김 성 연 (인)
위 원 윤 상 운 (인)

Abstract

Application of super-resolution imaging technique as an analytical tool

KIM HYUNG JUN
Major in Physical Chemistry
Department of chemistry
Seoul National University

Far-field microsocpy provide great advances to investigate structural and dynamic information of various sample system with low sample damage and high imaging contrast. Especially, Super-resolution technique is known as one of the innovative techniques in life sciences and material sciences because it enable to visualize nanoscopic structure of biological samples and materials. Since the sub-nanostructure of the sample determines their properties, developing the methods to analyze nanoscale structure directly is very important. Therefore, we try to establish a methodology to accurately measure biological molecules at a single unit level.

A combination of DNA stretching method and super-resolution nanoscopy allows an accurate and precise measurement of the length of DNA fragments ranging widely in size from 117 bp to 23,130 bp. *Bst*EII- and *Hin*dIII-treated λDNA fragments were stained with an intercalating dye and then linearly stretched on a coverslip by dynamic molecular combing. The image of individual DNA fragments was obtained by stimulated emission depletion nanoscopy. For DNA fragments longer than ~1,000 bp, the measured lengths of DNA fragments were consistently within ~0.5 to 1.0% of the reference values, raising the possibility of this method in a wide range of applications including facile detection for copy number variations and trinucleotide repeat disorder.

Mitochondria play a crucial role in maintaining cellular energy metabolism and various cellular function. Moreover, mitochondrial dysfunction is closely related with cellular senescence that may ultimately contribute to aging. Since

the sub-structure of mitochondria can reflect mitochondrial activity in various cellular environment, we apply super-resolution STED nanoscopy to show the morphological dispersion of mitochondria under the diffraction limit both in sub-cultured human primary skin fibroblasts and mouse skin tissues. In the sub-cultured fibroblasts, confocal microscopy provides overall morphology of mitochondrial membrane and indiscerptible TFAM location within diffraction limit. However, using super-resolution STED nanoscopy, we can resolve nanoscale distribution of TOM20 clusters and analyze quantitatively accurate number of nucleoids per cell in each sample condition. Similar results were shown for TOM20 distribution analysis in the mouse tissues. Our results suggested that the super-resolution technique based on fluorescence imaging can be useful to analyze structural difference of mitochondrial sub-structure in cells and tissues.

We report a water-soluble turn-on type diarylethene SO3-BPDBTEO that reversibly switches on/off its fluorescence upon light stimuli. We note that two sodium sulfonate groups enable SO3-BPDBTEO to exhibit excellent photoswithching properties in aqueous condition over a wide pH range between 3 and 10. It is demonstrated that SO3-BPDBTEO can be applied for the conventional fluorescence imaging of mammalian cell line such as HeLa cells at various pH conditions with low cytotoxicity. We also examine its feasibility for super-resolution resolution fluorescence imaging as a photoswitching probe.

Application of BALM (binding activated localization microcopy) was shown to allow facile imaging of amyloid fibrils with a typical diameter of ~14 nm FWHM. We also observed a twisted ribbon-like substructure of mutant amyloid fibrils and even what appear to be toxic amyloid oligomers with their characteristic morphological features consistent with TEM images. Use of an easily available staining dye in this method greatly enhances the prospect of addressing amyloid-related diseases in their diagnosis and drug tests by allowing facile *in situ* and *in vivo* detection by optical imaging.

……

Keywords **:** STED nanoscopy, Dynamic molecular combing, DNA,

mitochondria, photoswichable dye, super-resolution imaging.

Student Number **: 2011-30100**

Contents

Chapter 1. Direct and Precise Length Measurement of Single, Stretched DNA Fragments by Dynamic Molecular Combing and STED Nanoscopy

[This chapter was published in Analytical and Bioanalytical Chemistry, 408, 6453-6459 (2016).]

1.1 Introduction

Besides its main function to carry genetic information[1, 2], some DNAs have structural[3], regulatory[4], and enzymatic[5, 6] functions. X-ray diffraction[7], electron microscopy[8], and scanning probe microscopy[9] were used to study the structures of DNA, but imaging of a single DNA in biological environment remains a challenging goal to date. Optical microscopy was deemed unsuitable to observe an object less than in size the optical diffraction limit, λ/2NA ~200 nm (λ: wavelength of visible light, NA: numerical aperture), for over a century until the advent of super-resolution nanoscopy since the middle of the 1990's[10]. Recently, stimulated emission depletion (STED) nanoscopy and its variant ground state depletion (GSD) nanoscopy were respectively shown to achieve a lateral resolution of ~6 nm and 12 nm for a single colour centre in fluorescent nanodiamonds[11, 12], with a prospect of applications in wide ranging areas[13-15]. STED nanoscopy was also employed to image the intact form of λDNA on a poly-L-lysine coated coverslip with a spatial resolution of 45 nm, which is comparable to the persistence length of DNA[16].

Agarose gel electrophoresis has been widely used in biochemistry to measure the size distribution of DNA molecules by separating them by their electrostatic charge upon applying an electric potential[17, 18]. Despite its popularity and usefulness, it requires determination of agarose concentration and use of a ladder DNA to compare the size of sample DNAs. The upper limit of DNA size measurable with this technique is ~10 kbp at a reasonable resolution, which falls short to identify longer DNAs such as λDNA or chromosomal DNA[19]. Furthermore, one can only observe bands of an ensemble of DNA, but not single DNA

molecules.

On the other hand, fluorescence has been effectively used to measure the size of single DNA molecules. Goodwin et al. utilized flow cytometry to detect the fluorescence signal from individual fragments of flowing DNA[20]. Foquet et al. also measured the fluorescence burst from single DNA fragments using a microfluidic channel[21]. Laib et al. deduced the length of certain DNA fragments by comparing the brightness of the fluorescence signal assuming that it is proportional to the length of DNA[22]. Although these methods generally allow quick measurements, they are indirect in nature and often fraught with large standard deviations. In contrast, we introduce direct optical imaging by STED nanoscopy in this work to measure the length of individual DNA molecules linearly stretched on a coverslip.

DNAs can be stretched by using capillary force[23, 24], force flow[24], and dynamic molecular combing (DMC)[25-27]. DMC is simple and gives superior reproducibility. Short DNAs as well as longer ones including chromosomal DNA can be easily stretched. For comparison, we also used atomic force microscopy (AFM) to image the combed DNA on a glass substrate[9, 28, 29]. It is shown that our new method is highly accurate and precise.

1.2 Experimental Method

1.2.1 Sample Preparation

Initially, we tested the feasibility of dynamic molecular combing with a full sequence λDNA (48,502 bp, N3011S, New England Biolabs). A λDNA stock was diluted to 800 pM with TE buffer (10 mM Tris, 1 mM EDTA, 20 mM $MgCl_2$,100mMNaCl,pH7.4).10 μL of diluted sample was

incubated at 75°C for 15 min to prevent the adhesive ends of DNA from sticking to each other. The sample was then transferred to ice and incubated for 40 min with the addition of DNA-intercalating dimeric cyanine dye YOYO-1 (13 μM in TE buffer) to achieve the ratio of 1 dye per 5 base pairs. The brightness of the dye increased greatly (over 500 fold) upon binding to DNA[30]. After incubation, the sample was loaded in Teflon chamber to which 1.5 mL of TE buffer (10 mM Tris, 1 mM EDTA, 20 mM $MgCl_2$, 100mM NaCl, pH 7.4) was further added.

λDNA fragments (N3012S and N3014S, New England Biolabs) were diluted with TE buffer (10 mM Tris, 1 mM EDTA, 20 mM $MgCl_2$, 100mM NaCl, pH 7.4) by a factor of 20.10 μL of the sample DNA was mixed with 3 μL of YOYO-1 and left at room temperature for 40 min. After 40 min at room temperature, the mixture was added to 1.5 mL of TE buffer (10 mM Tris, 1 mM EDTA, 20 mM $MgCl_2$, 100mM NaCl, pH7.4) and loaded in Teflon chamber.

Since the exact concentration of the fragments was not known, we determined the optimal amount of dye through many trials. An excess amount of dye resulted in a low signal-to-noise (S/N) ratio due to the adhesion of free dyes on coverslip that appeared as background. On the other hand, an insufficient amount of dye yielded poor image quality with many dark spots along the DNA strands. In our experiment, we predicted that YOYO-1 would bind to *Bst*EII or *Hin*dIII-treated λDNA at a similar dye-per-base pair ratio as in the full sequence λDNA experiment. YOYO-1 dye is known to bind to a single-stranded as well as double-stranded DNA. Therefore, although the sticky ends have a length of about 12 bps for the whole λDNA, 5 bps for *Bst*EII- treated λDNA, and 4 bps for *Hin*dIII-treated λDNA, they all can be observed by

imaging.

1.2.2 Silanization of Coverslips

A coverslip was washed with acetone, transferred into a beaker, sonicated for 20 min in a 1:1 mixture of deionized water and methanol, and sonicated again in chloroform for another 20 min. To clean the surface of coverslip, it was treated with piranha solution (a 7:3 mixture of 98 % sulfuric acid and 35% hydrogen peroxide, Sigma) for at least 2 hours in a water bath kept at 65°C until all bubbles disappeared. The coverslip was then transferred to a clean beaker with Teflon tweezers, where it was alternately sonicated in chloroform and deionized water. The final treatment was done in chloroform to keep the hydrophobic surface intact. The coverslip was transferred to a new beaker containing 100 mL of n-heptane, where 100 μL of trimethoxy(7-octen-1-yl)silane (Sigma) was added and incubated overnight while moisture was removed with Drierite (Sigma). The coverslip was recovered and sonicated in *n*-heptane, deionized water and chloroform, sequentially for 5 min, and stored in a dry jar with Drierite.

1.2.3 Dynamic Molecular Combing

A silanized coverslip was immersed in the Teflon chamber containing the sample DNA[31]. After 5 min, the coverslip was constantly pulled up at a speed of 200 μm/sec (Figure. 1) using a glass extraction system adapted from syringe pump, to control the pull-up speed mechanically. A longer incubation time in Teflon chamber resulted in the sticking of both adhesive ends of DNA to coverslip, hampering the normal combing process. The pull-up speed also affects the quality of DNA stretching (Figure. 2 Top and Figure. S1). After the pull-up step, the coverslip was placed on a slide glass and mounted with 97%

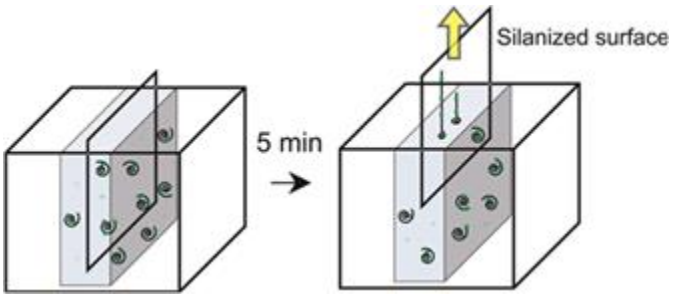

Figure. 1 Schematic representation of dynamic molecular combing. A solution containing DNA labelled with YOYO-1 was transferred to a Teflon chamber. A silanized coverslip was immersed in the solution and left there for 5 min. The coverslip was then pulled up at a speed of 200 μm/sec to yield linearly stretched DNA on the coverslip.

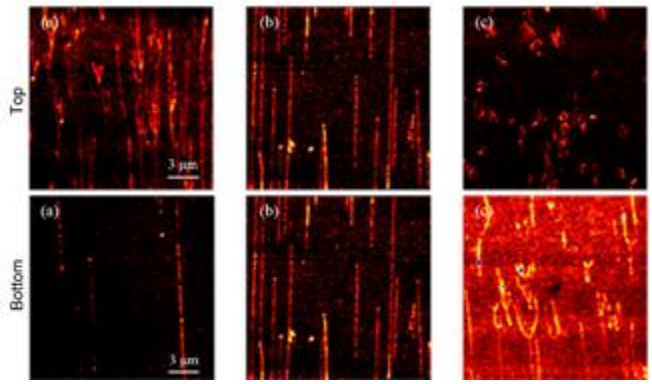

Figure. 2 (Top) Comparison of the linearity of combed λDNA using different pull-up speeds: (a) 20 μm/sec, (b) 200 μm/sec, and (c) 1,000 μm/sec. (Bottom) Comparison of the image brightness of combed λDNAs using different ratio of dye per base pair in the MES buffer. (a) 1:30, (b) 1:5, and (c) 1:1.

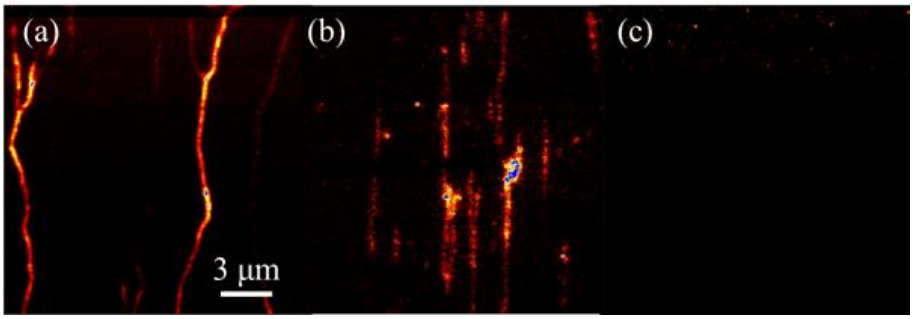

Figure S1. Comparison of the linearity of combed λDNAs at a pull-up speed of (a) 30 μm/sec, (b) 200 μm/sec, and (c) 400 μm/sec.

2, 2'-Thiodiethanol (Sigma). Nail polish was used to prevent leakage of TDE. Mercaptoethanolamine and trolox were added to reduce photobleaching and photoblinking.

1.2.4 STED Nanoscopy

Our pulsed-CW STED nanoscopy system is schematically shown in Figure. 3. A super-continuum light was generated from the 800 nm output of a Ti-Sapphire laser (<100 fs, 80 MHz, Mai Tai HP, Spectra-Physics) by a photonic crystal fiber (FemtoWhite800, NKT Photonics). An excitation filter (FL488-10, Thorlabs) was used to select light at 488 nm that was used as an excitation source (2 μW at focal plane to minimize photobleaching by the excitation beam). For stimulated emission depletion, we used a strong CW output (120 mW at focal plane) of a 592 nm laser (2RU-VFL-P-1500-592, MPB Communications). The two beams propagated collinearly after reflection at dichroic mirrors and became circularly polarized by half- and quarter-wave plate, considering the random orientation of the dipole of the dyes. The STED beam passed through a phase mask (VPP-1a, RPC Photonics) and became a doughnut shape at focal plane. The excitation beam was made to overlap with the doughnut-shaped STED beam at the focal point. No synchronization was necessary since we used a CW STED beam. An oil immersion type objective (HCX PL APO, 100X, 1.4 NA, Leica) was used to focus the two beams and to collect fluorescence through a home-built inverted confocal fluorescence microscope. The sample area was scanned by a piezo stage (NanoMax-TS, Thorlabs) and the fluorescence signal was detected by an avalanche photodiode detector (SPCM-AQR-14-FC, Perkin Elmer) after passing through an emission filter (FF01-530/55-25, Semrock). We obtained images repeatedly at the same position and found that each object appeared at exactly

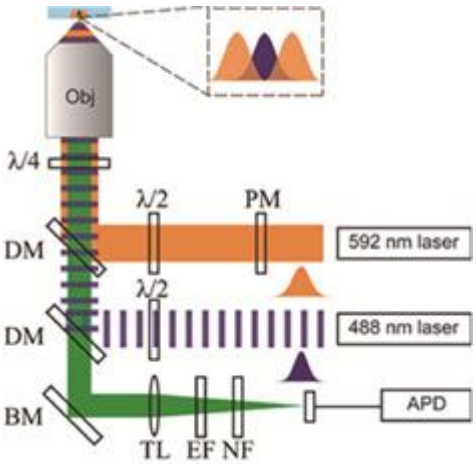

Figure. 3 Schematic of our pulsed-CW STED nanoscopy system. PM: phase mask, λ/2: half-wave plate, λ/4: quarter-wave plate, DM: dichroic mirror, BM: broadband mirror, Obj: objective lens, TL: tube lens, EF: emission filter, NF: notch filter, APD: avalanche photodiode.

the same position, which indicates that spatial drifting due to the piezo stage was negligible. The strong CW STED beam was blocked by a 594 nm notch filter (NF03-594E-25, Semrock). The imaging acquisition time for an area of 18 μm x 18 μm was less than 30 s. Imaging and post-imaging processes were performed with the software programs *Imspector* and *Image J*. Line profiles of DNA strands were obtained from the image and the end-to-end length based on the point spread function of our STED scheme was automatically calculated.

1.2.5 Determination of elongation factor

According to Ref. 34, the elongation factor is the ratio of stretched vs. unstretched lengths of a molecule. The stretched length originates from DMC and is measured by STED, while the unstreched length, the length in physiological aqueous solution, is calculated from the number of bp (1 bp = ~0.34 nm). Therefore, if we change the experimental conditions such as the pull-up speed or pH of DNA solution, the elongation factor may change. The reference values in Tables 1 and 2 are the numerical product of (the number of bp) x (the unit base pair length of 0.34 nm) x (the elongation factor of 1.5 empirically determined for our experiment).

1.3 Results & Discussion

The top panel of Figure. 4 shows whole-area confocal and STED images of the *Bst*EII-treated λDNA fragments linearly stretched, while the bottom panel compares the same images in a more densely populated region of DNA fragments. With the STED beam on, the fluorescence from YOYO-1 was almost completely depleted except in the central

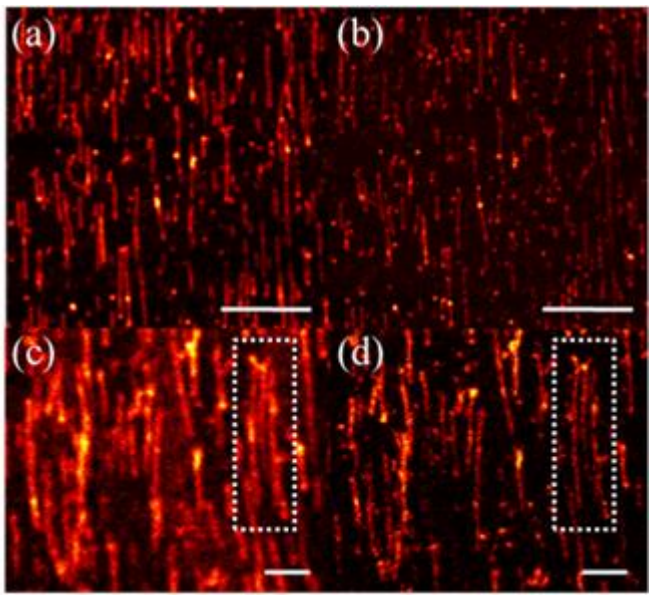

Figure. 4 Top: Whole-area images by (a) confocal and (b) STED microscopy for combed λDNA fragments digested with *Bst*EII restriction enzyme. λDNA fragments were stained with YOYO-1, an intercalating dye, and stretched on a coverslip by dynamic molecular combing. Image size: 18 μm x 18 μm. Scale bar: 5 μm. Bottom: Local images by (c) confocal and (d) STED microscopy for a more densely populated region of DNA fragments. The 3 strands in the white box are shown to be clearly resolved in the STED image. Scale bar: 1 μm.

part where the STED beam intensity was nearly zero. No spatial drifting induced by piezo stage was detected. The FWHM of our STED images was reduced maximally by 5 times to ~47 nm from that of confocal images (~240 nm, Figure. 5 and Figure. S5). Statistically, STED nanoscopy improved the resolution of DNA images by 4 times according to Figure. S5 in ESM. Some of the very closely placed DNA fragments that are not fully resolved by confocal imaging can be readily distinguished by STED imaging (white boxes in the bottom panel of Figure. 4).

The density of the combed DNA showed strong dependence on pH and salt concentration. In our case, DNA fragments were most densely combed at pH 7.4 and salt concentration of 20 mM $MgCl_2$ and 100 mM NaCl (Figure. S2 and S3). Most of DNA fragments were well stretched linearly by DMC, but we also found a small number of fragments that were U-shaped or crooked. The U-shaped fragments result from those which stick to the surface of the coverslip at two ends before pulling, while the crooked ones appear to be formed during the combing process as the hydrophobic interaction of DNA base with the silanized surface of coverslip changes as DNA is pulled. The concentration of YOYO-1 also affects the quality of the image (Figure. 2 Bottom; see also electronic supplementary material Figure. S4). At a low concentration, a large number of dark regions appear along strands, which makes it difficult to identify intact fragments. At high concentrations, the S/N ratio suffers, but the concentration of YOYO-1 little affects the spatial resolution itself.

Since the pulse-CW STED scheme generally has low depletion efficiency due to the unintended temporal overlap of the two beams and

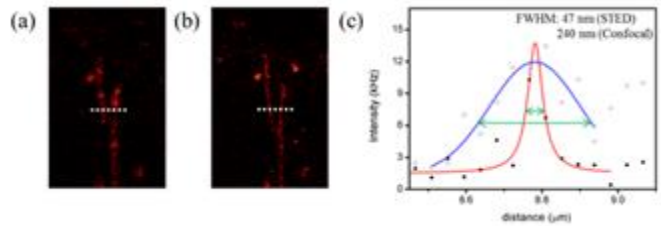

Figure. 5 FWHM lateral width of (a) confocal vs. (b) STED images, with (c) their line profiles along the white dashed lines fitted by Gaussian (confocal) and Lorentzian (STED) curve. Because of the low spatial resolution of the confocal image, the signal intensity to the right side of the peak (at distance > ~8.8 μm) is due to a nearby fragment.

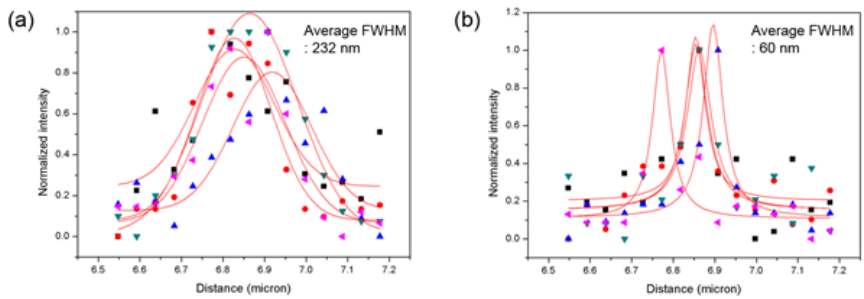

Figure S5. Line profiles used to determine the FWHM lateral width of (a) confocal vs. (b) STED images. The lines are fitted by Gaussian (confocal) and Lorentzian (STED) curve.

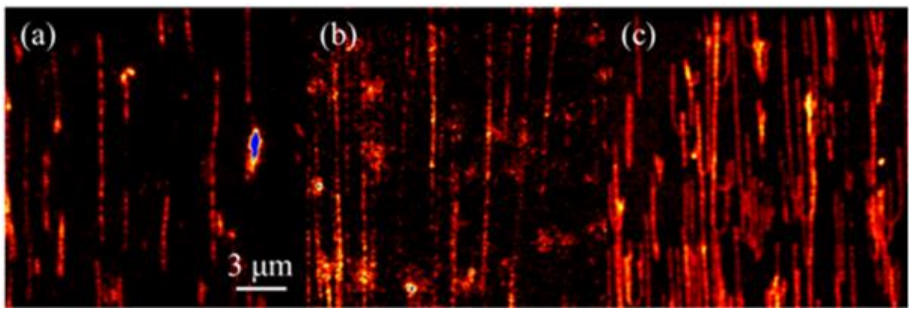

Figure S2. Comparison of the density of combed λDNAs under different buffer conditions: (a) MES buffer at pH 4.5, (b) MES buffer at pH 5.5, and (c) TE buffer at pH 7.4.

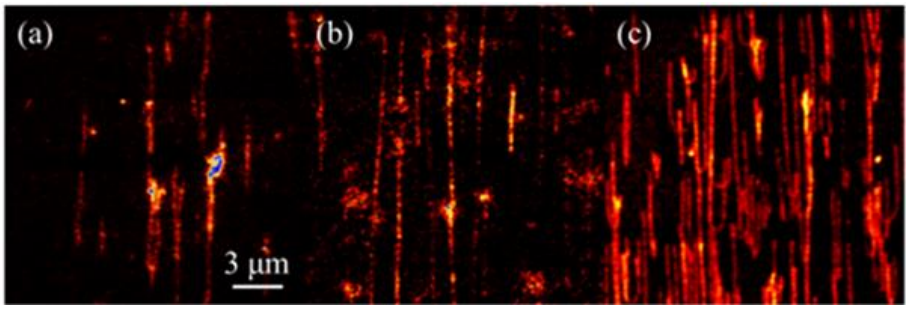

Figure S3 Comparison of the density of combed λDNAs at different salt concentrations in the TE buffer. (a) without salt, (b) 100 mM NaCl, and (c) 20 mM $MgCl_2$ and 100 mM NaCl.

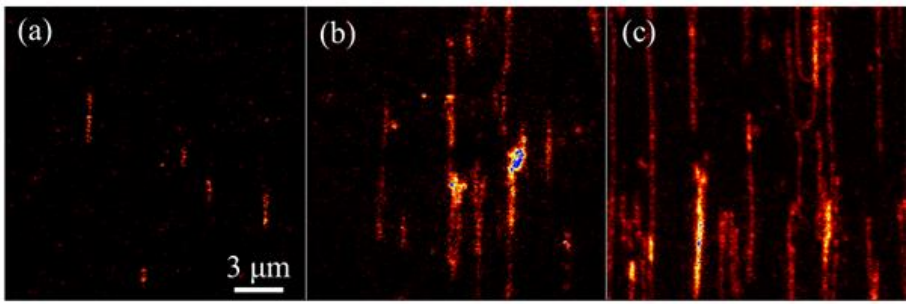

Figure S4. Comparison of the image brightness of combed λDNAs using different ratio of dye per base pair in the MES buffer: (a) 1:20, (b) 1:10, and (c) 1:5.

the continuous irradiation of the STED beam, a strong intensity of the latter is needed to achieve a similar performance to the pulse-pulse STED scheme. A possible danger with using a strong STED beam is the photobleaching of YOYO-1, which would lead to a disrupted image of DNA along its strand. In order to avoid this problem, the average power of the STED beam was adjusted to 120 mW at focal plane and the dwell time per pixel never exceeded 100 μs and mainly remained at 75 μs, to obtain a typical photon count of about 30~50 per pixel. A shorter dwell time may be used to completely avoid photobleaching at the expense of a low S/N ratio[32]. Of course, another alternative would be to use a pulsed STED beam, which requires synchronization with the excitation beam but would definitely improve the resolution without much risk of photobleaching. We also used a minimum power of the excitation beam (2 μW) as it affected the degree of photobleaching. When we obtain confocal and STED images from the same region for comparison, we always obtain the confocal image first to avoid photobleaching by the STED beam[33].

Figures 6 and 7 show the size distribution of DNA fragments treated with *Bst*EII and *Hin*dIII, respectively. It is known that the distance between two adjacent base pairs is considerably increased with DMC by a factor of up to ~2 depending on various experimental conditions such as the substrate for DMC, shear strength of the adsorbed DNA, and adhesion energy at the DNA-surface interface[27]. In our case, this elongation factor is estimated to be ~1.5 by an analytical approximation[34], yielding an interpair distance of ~0.5 nm. When we converted the measured lengths of DNA fragments into the number of base pairs using this value, the result was in excellent agreement,

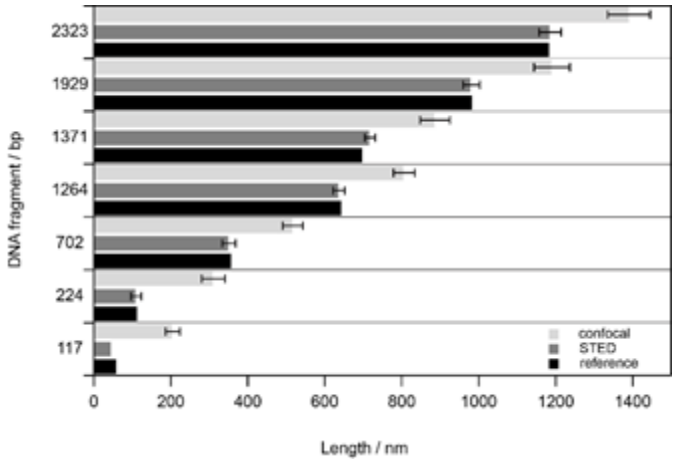

Figure. 6 Histogram for the size distribution of *Bst*EII-treated λDNA fragments. Each horizontal panel gives the length of a DNA fragment measured by confocal microscopy (top, light gray bar) and STED nanoscopy (middle, gray bar) along with the reference value provided by the manufacturer (bottom, black bar). An excellent agreement between the STED and reference values are consistently seen, whereas the confocal values tend to be far off, relatively more so for shorter fragments. For each fragment, 20 DNA strands were analysed and averaged for the length measurement.

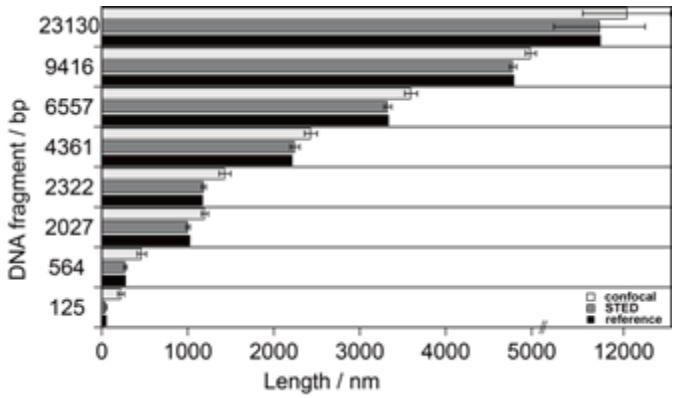

Figure. 7 Histogram for the size distribution of *Hin*dIII-treated λDNA fragments. Each horizontal panel gives the length of a DNA fragment measured by confocal microscopy (top, light gray bar) and STED nanoscopy (middle, gray bar) along with the reference value provided by the manufacturer (bottom, black bar). An excellent agreement between the STED and reference values are consistently seen, whereas the confocal values tend to be far off, relatively more so for shorter fragments.

perhaps fortuitously but at least consistently, with the reference values provided by the manufacturer of our sample (Table 1 and 2). More details of the elongation factor are given in ESM.

The result in Figure. 6 and 7 represent that a combination of DMC and STED nanoscopy was demonstrated to accurately and precisely analyze the lengths of DNA widely ranging in size from 117 bp to 23,130 bp. (The maximum length of DNA to measure with our current setup is 35,294 bp, which is imposed by the maximum travel distance (18 μm x 18 μm) of our piezo stage in the scanning device.) In particular, the ability to distinguish 1,264 bp from 1,371 bp as well as 117 bp from 224 bp is sufficient evidence to prove the feasibility of this new method in copy number variation assay.

To further verify the accuracy of the length determination by DMC-STED, we performed tapping mode AFM measurements for both intact λDNA and fragmented λDNA on identical coverslip surface. We found that the lengths from AFM measurement agree very well with the reference values as well as our STED measurement (Figs. 8, 9 and Table 2). Compared with STED, AFM requires a much longer acquisition time and can also damage the stretched DNAs on a coverslip due to the direct interaction between the AFM tip and the DNAs. Actually, we found that some stretched DNAs broke as we measured the morphology of DNAs fixed on a coverslip by AFM.

We note that the STED results are not only much more “accurate” (closer to the reference values) but also more “precise” (with smaller standard deviations) than the confocal values. The point spread function of our STED system is ~50 nm, which may largely account for the small discrepancy between the STED-measured vs. actual length. For DNA

Confocal (in nm) (standard deviation)	4,988 (121)	3,597 (146)	2,433 (147)	1,433 (135)	1,200 (76)	466 (102)	225 (72)
STED (in nm) (standard deviation)	4,784 (82)	3,327 (86)	2,247 (110)	1,187 (51)	1,004 (46)	275 (34)	50 (14)
Reference (in nm)	4,802	3,344	2,224	1,184	1,034	288	64
STED/ Reference ratio (in %)	99.63	99.49	101.0	100.3	97.10	95.49	78.13

Table 1 Comparison of the lengths of *Hin*dIII-treated λDNA fragments experimentally measured by confocal microscopy (top row) and STED nanoscopy (second row) along with the reference values provided by the manufacturer (third row). The STED results are much more accurate (closer to the reference values, shown by the excellent STED/Reference ratios given in the bottom row) and precise (with smaller standard deviations) than the confocal values. DNA fragments as short as 50 nm (~100 bp) can be easily measured and discriminated in size by STED nanoscopy, in strong contrast to confocal microscopy.

AFM (in nm) (standard deviation)	1,187 (60)	972 (52)	700 (33)	639 (16)	358 (29)	123 (13)	58 (10)
STED (in nm) (standard deviation)	1,186 (57)	981 (43)	718 (27)	637 (30)	351 (35)	110 (27)	45 (0)
Reference (in nm)	1,185	984	699	645	358	114	60

Table 2 Comparison of the lengths of *Bst*EII-treated λDNA fragments experimentally measured by AFM (first row) and STED nanoscopy (second row) along with the reference values provided by the manufacturer (third row). The lengths from AFM measurement agree very well with the reference values as well as our STED measurement.

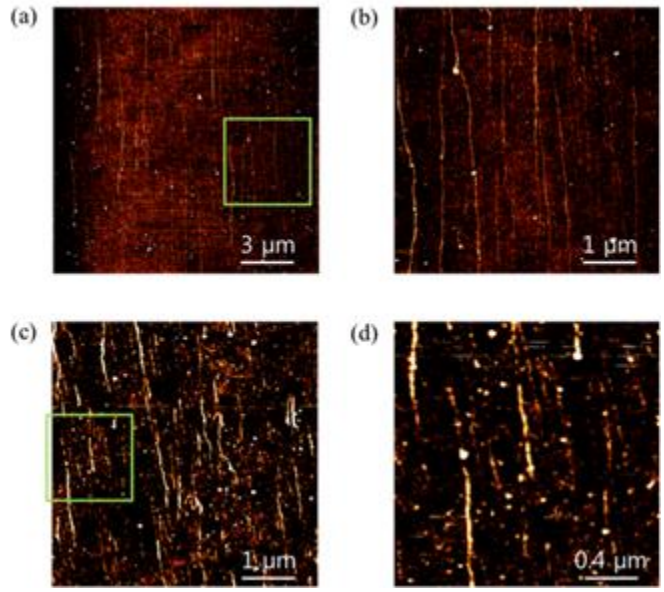

Figure. 8 Tapping mode AFM images of (a) combed λDNA (15 μm x 15 μm) and (b) enlarged image of green-boxed region of (a). AFM images of (c) combed λDNA fragments digested with *Bst*EII restriction enzyme and (d) enlarged image of green-boxed region of (c).

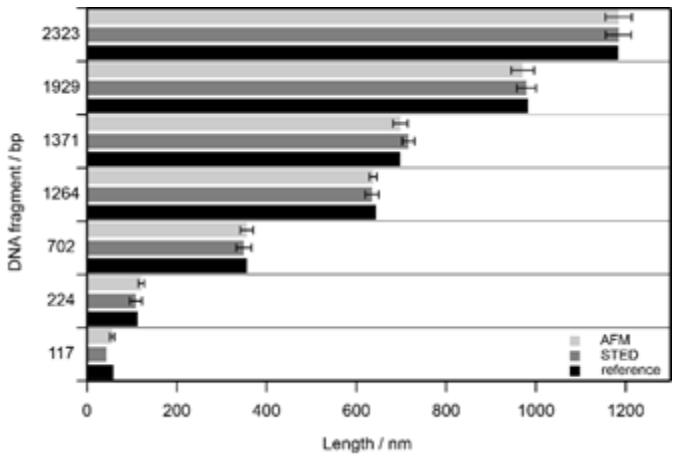

Figure. 9 Histogram for the size distribution of *Bst*EII-treated λDNA fragments. Each horizontal panel gives the length of a DNA fragment measured by AFM (top, light gray bar) and STED nanoscopy (middle, gray bar) along with the reference value provided by the manufacturer (bottom, black bar). An excellent agreement among AFM, STED and reference values is consistently seen.

fragments longer than ~1,000 bp, the ratio of the STED vs. reference values ranges from 99.49% to 101.03%. The strength of our DMC-STED method is that DNA fragments ranging widely in size from 117 bp to 23,130 bp could be stretched and identified at once in a single image.

Determination of the size of DNA can be utilized in the diagnosis of the genetic disorder caused by copy number variation (CNV). Unlike single nucleotide polymorphism (SNP) caused by alterations of a single base in the genome sequence, CNV results from certain fragments of the sequence entirely missing or duplicated, yielding copies of DNA different in total length regardless of specific sequence information. Recently, Baday et al. designed a CNV detection scheme using two-color SHRImP and SHREC[35]. They were able to resolve two probes 32 nm apart from each other, but had to modify their DNA to covalently conjugate additional dye molecules (TAMRA, Cy3 and Cy5) outside the DNA backbone, which itself was stained with YOYO-1. By comparison, our method does not need such DNA modification or fluorophore conjugation since we measure directly the size of DNA, not the distance between the single probes.

1.4 Conclusion

In summary, by using the combined method of DMC and STED nanoscopy, we demonstrated the feasibility of measuring the length of individual DNA fragments linearly stretched on a coverslip. With this method, the lengths of DNA fragments widely ranging size could be measured accurately and precisely by super-resolution imaging, with no need for elaborate covalent conjugation steps for fluorescent dye since the intercalating dye we used can

fluorescently stain DNA simply by mixing with them. Possible applications to CNV detection and diagnosis of trinucleotide disorder are anticipated.

1.5 Reference

1. Crick FH. On protein synthesis. Symp Soc Exp Biol. 1958;12:138-63.

2. Crick F. Central dogma of molecular biology. Nature. 1970;227(5258):561-3.

3. Marmorstein LY, Kinev AV, Chan GK, Bochar DA, Beniya H, Epstein JA et al. A human BRCA2 complex containing a structural DNA binding component influences cell cycle progression. Cell. 2001;104(2):247-57.

4. Preston CM, Frame MC, Campbell ME. A complex formed between cell components and an HSV structural polypeptide binds to a viral immediate early gene regulatory DNA sequence. Cell. 1988;52(3):425-34.

5. Sen D, Geyer CR. DNA enzymes. Curr Opin Chem Biol. 1998;2(6):680-7.

6. Silverman SK. In vitro selection, characterization, and application of deoxyribozymes that cleave RNA. Nucleic Acids Res. 2005;33(19):6151-63.

7. Raghunathan S, Ricard CS, Lohman TM, Waksman G. Crystal structure of the homo-tetrameric DNA binding domain of Escherichia coli single-stranded DNA-binding protein determined by multiwavelength x-ray diffraction on the selenomethionyl protein at 2.9-angstrom resolution. P Natl Acad Sci USA. 1997;94(13):6652-7.

8. Griffith J, Bleyman M, Rauch CA, Kitchin PA, Englund PT. Visualization of the Bent Helix in Kinetoplast DNA by Electron-Microscopy. Cell. 1986;46(5):717-24.

9. Hu J, Wang M, Weier HUG, Frantz P, Kolbe W, Ogletree DF et al. Imaging of Single Extended DNA Molecules on Flat (Aminopropyl)triethoxysilane−Mica by Atomic Force Microscopy. Langmuir.

1996;12(7):1697-700.

10. Hell SW, Wichmann J. Breaking the diffraction resolution limit by stimulated emission: stimulated-emission-depletion fluorescence microscopy. Opt Lett. 1994;19(11):780-2.

11. Rittweger E, Han KY, Irvine SE, Eggeling C, Hell SW. STED microscopy reveals crystal colour centres with nanometric resolution. Nat Photon. 2009;3(3):144-7.

12. Han KY, Kim SK, Eggeling C, Hell SW. Metastable dark States enable ground state depletion microscopy of nitrogen vacancy centers in diamond with diffraction-unlimited resolution. Nano Lett. 2010;10(8):3199-203.

13. Heller I, Sitters G, Broekmans OD, Farge G, Menges C, Wende W et al. STED nanoscopy combined with optical tweezers reveals protein dynamics on densely covered DNA. Nat Methods. 2013;10(9):910-U132.

14. Hanne J, Falk HJ, Gorlitz F, Hoyer P, Engelhardt J, Sahl SJ et al. STED nanoscopy with fluorescent quantum dots. Nat Commun. 2015;6. doi:ARTN 712710.1038/ncomms8127.

15. Bianchini P, Peres C, Oneto M, Galiani S, Vicidomini G, Diaspro A. STED nanoscopy: a glimpse into the future. Cell Tissue Res. 2015;360(1):143-50.

16. Persson F, Bingen P, Staudt T, Engelhardt J, Tegenfeldt JO, Hell SW. Fluorescence nanoscopy of single DNA molecules by using stimulated emission depletion (STED). Angew Chem Int Ed Engl. 2011;50(24):5581-3.

17. Kryndushkin DS, Alexandrov IM, Ter-Avanesyan MD, Kushnirov VV. Yeast [PSI+] prion aggregates are formed by small Sup35 polymers fragmented by Hsp104. J Biol Chem. 2003;278(49):49636-43.

18. Sambrook J, Russell DW. Molecular Cloning: A Laboratory Manual CSHL press; 2001.

19. Stanojcic S, Sollelis L, Kuk N, Crobu L, Balard Y, Schwob E et al. Single-molecule analysis of DNA replication reveals novel features in the divergent eukaryotes Leishmania and Trypanosoma brucei versus mammalian cells. Sci Rep-Uk. 2016;6. doi:ARTN 2314210.1038/srep23142.20. Goodwin PM, Johnson ME, Martin JC, Ambrose WP, Marrone BL, Jett JH et al. Rapid sizing of individual fluorescently stained DNA fragments by flow cytometry. Nucleic Acids Res. 1993;21(4):803-6.

21. Foquet M, Korlach J, Zipfel W, Webb WW, Craighead HG. DNA fragment sizing by single molecule detection in submicrometer-sized closed fluidic channels. Anal Chem. 2002;74(6):1415-22.

22. Laib S, Rankl M, Ruckstuhl T, Seeger S. Sizing of single fluorescently stained DNA fragments by scanning microscopy. Nucleic Acids Res. 2003;31(22):e138.

23. Otobe K, Ohtani T. Behavior of DNA fibers stretched by precise meniscus motion control. Nucleic Acids Res. 2001;29(22):E109.

24. Chan TF, Ha C, Phong A, Cai D, Wan E, Leung L et al. A simple DNA stretching method for fluorescence imaging of single DNA molecules. Nucleic Acids Res. 2006;34(17):e113. doi:10.1093/nar/gkl593.

25. Michalet X, Ekong R, Fougerousse F, Rousseaux S, Schurra C, Hornigold N et al. Dynamic molecular combing: stretching the whole human genome for high-resolution studies. Science. 1997;277(5331):1518-23.

26. Gueroui Z, Place C, Freyssingeas E, Berge B. Observation by fluorescence microscopy of transcription on single combed DNA. Proc Natl Acad Sci U S A. 2002;99(9):6005-10.

27. Benke A, Mertig M, Pompe W. pH- and salt-dependent molecular combing of DNA: experiments and phenomenological model. Nanotechnology. 2011;22(3):035304.

28. Deng Z, Mao C. DNA-Templated Fabrication of 1D Parallel and 2D Crossed Metallic Nanowire Arrays. Nano Letters. 2003;3(11):1545-8.

29. Hu J, Zhang Y, Gao H, Li M, Hartmann U. Artificial DNA Patterns by Mechanical Nanomanipulation. Nano Letters. 2002;2(1):55-7.

30. Figeys D, Arriaga E, Renborg A, Dovichi NJ. Use of the fluorescent intercalating dyes POPO-3, YOYO-3 and YOYO-1 for ultrasensitive detection of double-stranded DNA separated by capillary electrophoresis with hydroxypropylmethyl cellulose and non-cross-linked polyacrylamide. Journal of Chromatography A. 1994;669(1–2):205-16.

31. Labit H, Goldar A, Guilbaud G, Douarche C, Hyrien O, Marheineke K. A simple and optimized method of producing silanized surfaces for FISH and replication mapping on combed DNA fibers. Biotechniques. 2008;45(6):649-52, 54, 56-8.

32. Wu Y, Wu X, Lu R, Zhang J, Toro L, Stefani E. Resonant Scanning with Large Field of View Reduces Photobleaching and Enhances Fluorescence Yield in STED Microscopy. Sci Rep. 2015;5:14766.

33. Klar TA, Jakobs S, Dyba M, Egner A, Hell SW. Fluorescence microscopy with diffraction resolution barrier broken by stimulated emission. Proc Natl Acad Sci U S A. 2000;97(15):8206-10.

34. Bensimon D, Simon AJ, Croquette VV, Bensimon A. Stretching DNA with a receding meniscus: Experiments and models. Phys Rev Lett. 1995;74(23):4754-7.

35. Baday M, Cravens A, Hastie A, Kim H, Kudeki DE, Kwok P-Y et al. Multicolor Super-Resolution DNA Imaging for Genetic Analysis. Nano Letters. 2012;12(7):3861-6.

Chapter 2. Visualization of Structural Difference of Mitochondria by UV exposure in Dermal Cells and Tissues Using STED Nanoscopy as an Analytical Technique

2.1 Introduction

Mitochondria, as the powerhouse of the cell, are vital organelles in indispensable lipid membrane metabolism pathways such as respiratory ATP production[1]. Mitochondria form a dynamic reticulum of long, thin, and branched tubular networks which show an extensive geometries depending on the types of cell and environmental conditions and spread throughout the cytoplasm of the cell[2].

In eukaryotes, oxidative phosphorylation process occurs in the mitochondria which is an organelle bound by inner and outer membranes. They surround a dense matrix that contains enzymes involved intermediate metabolism and numerous copies of a genome that encodes for partial proteins on the inner membrane and the RNAs required for their translation[6].

In disease, the function of mitochondria has been expanded the role in the respiratory chain into the defects on extra mitochondrial roles. Moreover, its behaviors have been linked to metabolic disorders and neurodegenerative diseases such as Alzheimer's and Parkinson's disease[3,4]. For example, the defects in the oxidative phosphorylation system assembly on cristae give rise to numerous serious human diseases[5].

Although the overall architecture and major function of mitochondria have been described progressively, our current understanding of the fundamental correlation between mitochondria and disease is still poor. It needs a better understanding of the molecular components that determine the mitochondrial structure, as well as the connections between mitochondria and extra-mitochondrial pathways in various cell types at the cell organelle level[3].

As the mitochondrial theory for aging has been one of the most convincing aging theories, it is closely related with mitochondrial dysfunction on electron

transport chain involving free radical generation. Recent observation has implicated that aging-dependent decrease of mitochondrial complex II, one of the mitochondrial complexes associated with electron transport chain, activity in human dermal fibroblasts is involved in the aging process[7]. Since the mitochondria are the leading manufacturers of both cellular energy and free radicals, dysfunctional mitochondria are particularly thought to induce the considerable decline of critical muscle function[8].

Fission and fusion play crucial roles in maintaining mitochondrial functions when cells undergo metabolic or environmental stresses. Fission is necessary to produce new mitochondria, but it also could contribute to remove damaged mitochondria and induce apoptosis by extreme cellular stress. Fusion helps to reduce stress by mixing the components in partially damaged mitochondria as the complementation process[9].

Progressive accumulation of oxidative damage, mostly occurred by mitochondrial dysfunction, is one of the significant factors for aging. Reactive oxygen species (ROS) can consequently lead to cellular senescence[10]. Oxidative stress can be caused by various stimuli such as UV[11], H_2O_2[12], and dopamine[13].

It has been known that oxdative stress induces cellular senescence in even in the early passage of human fibroblast[14-16]. Because the method for developing the cells having senescent features within a short period is well defined, the biological sample consisting of oxidatively stressed cells is a useful model system to study the fundamental mechanism and markers of senescence-associated response in aging[12].

For recent decades, far-field optical microscopy has positioned as an major technology to study cellular components both in structural and functional

terms[17]. But, the optical resolution is limited to ~200 nm by diffraction[18,19]. Particularly, a major challenge to understand the localization of mitochondrial proteins in cells is that mitochondrial components have less diameter than the resolution limit of conventional diffraction-limited microscopy, largely constraining the use of it to study submitochondrial protein distributions. Therefore, super-resolution imaging is the most suitable approach for quantitatively analyzing the distribution of proteins in mitochondria.

Using 3D STORM, they visualized the structure of the mitochondrial network and the spatial relevance between mitochondria and microtubules in cells[20]. Other group found that mitochondrial inner membrane organizing system is localized at the junctions of cristae, and that its clusters show an ordered distribution on the mitochondrial inner membrane that depend on the location of the mitochondria in the cell and on the orientation of the growth cellular surface using STED nanoscopy[21]. Using STED for the mapping of Percoll-purified mitochondrial proteins from murine heart, they were able to quantify and resolve distinct protein clusters within mitochondria[22]. Recently, super-resolution microscopy proposed the potential to explore the undeveloped nanoscale regime in tissues kept in a long term storage for biological specimens[23].

Mitochondria play a central role in maintaining cellular energy metabolism and various cellular function. Moreover, the dysfunction of mitochondria is related with cellular senescence that may ultimately contribute to aging. Since the sub-structure of mitochondria can reflect mitochondrial activity in various cellular environment, we demonstrate the feasibility of super-resolution STED nanoscopy as an analysis tool to estimate aging through visualizing the morphological dispersion of mitochondria under the diffraction limit both in sub-cultured human primary skin fibroblasts and mouse skin tissues.

2.2 Experimental Method

2.2.1 STED nanoscopy

For TOM20 (translocase subunit of mitochondria outer membrane) cluster analysis, we used custom-built STED nanoscopy for both confocal and STED images (Figure 1). The fluorophore STAR635P was excited with a light at 635 nm that was selected by an excitation filter (z635/10x, Chroma) from a super-continuum light source generated by the 780 nm output from a Ti-Sapphire laser (80 MHz, <100 fs, Mai Tai HP, Spectra-Physics) by a photonic crystal fiber (FemtoWhite, NKT photonics). Stimulated emission depletion was performed using the same laser operating at 780 nm with a repetition rate at 80 MHz. We synchronized the two beams and adjusted the time delay between excitation beam and STED beam to 180 ps. The STED beam become a doughnut shape at the focal plane passing through a polymeric phase mask (VPP-1a, RPC Photonics). A 100X oil immersion type objective (HCX PL APO, 1.4 NA, Leica) was used to focus the two beams and to collect fluorescence signal. A piezo stage (NanoMax-TS, Thorlabs) scanned the sample area and an avalanche photodiode (SPCM-AQR-14-FC, Perkin Elmer) detected the fluorescence. To avoid the saturation by high power of STED beam and eliminate the background signal, we arranged IR block filter (FF01-720/SP-25, Semrock) and emission filters (ET655LP, Chroma) in front of the detector. Image acquisition process were controlled by Imspector software. Confocal and STED images were obtained at the same position.

For TFAM (mitochondrial transcription factor A) quantitative analysis, both confocal and STED images were acquired on a Leica TCS SP8 microscope. 488 nm excitation source was used for Alexa488 fluorophore. A high power of CW laser at 592 nm was selected for switching off the fluorescence to

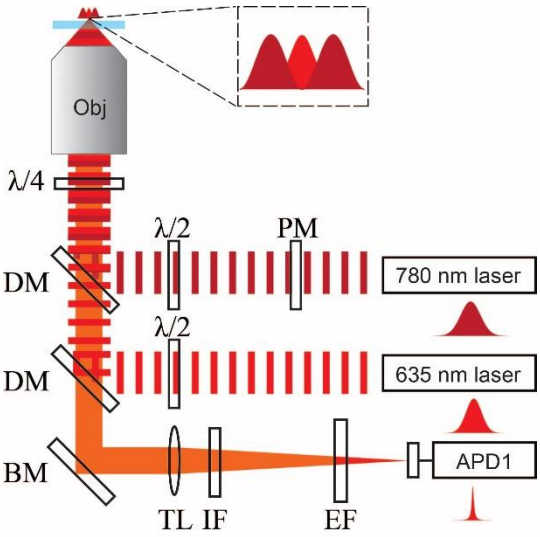

Figure 1. Schematic of our pulsed STED nanoscopy system. PM: phase mask, λ/2: half-wave plate, λ/4: quarter-wave plate, DM: dichroic mirror, BM: broadband mirror, Obj: objective lens, TL: tube lens, EF: emission filter, IF: IR block filter, APD: avalanche photodiode.

improve the spatial resolution. Image acquisition process were controlled by Leica application suite X software.

2.2.2 UV irradiated cell preparation and staining

Skin primary fibroblast from patient samples were isolated and sub-cultured for imaging. Sub-cultured fibroblasts were exposed to UV irradiation to induce UV-mediated skin damage to change the structure of mitochondria. Fibroblasts were fixed with paraformaldehyde and stained. Antibodies for TOM20 (translocase of mitochondrial outer membrane) and TFAM (mitochondrial transcription factor A) were used for labeling mitochondrial proteins. Alexa488 conjugated secondary antibodies and STAR635P conjugated secondary antibodies were used for fluorescence detection. After immunolabeling, the samples were mounted in prolong gold with DAPI.

Mitochondria were specifically targeted using anti-Tom20 (rabbit, Abcam) and subsequently labeled using Anti-rabbit-IgG-Star635P (Abberior). Polyclonal rabbit antibodies against Tom20 (Santa Crus biotechnology), goat anti-rabbit secondary antibodies (Jackson ImmunoResearch Laboratories)

2.2.3 Tissue preparation and staining

Tissues from skin of SKH-1 hairless mice were harvested. The skin tissues from mice were embedded with paraffin and cut with microtome to prepare 4 micron thick section. To dissolve paraffin, first of all, the sections were baked for 30 minutes in 65°C oven. The sections were washed by Xylene I, II, 100%, 95%, 80%, 70% EtOH, distilled water each for 5 minutes to dissolve paraffin and to rehydrate the tissue sections. The tissue sections were boiled with 100 mM sodium citrate by microwave for 5 minutes due to antigen retrieval. after cooling the sections down for 30 minutes, the samples were

washed three times with PBS and permeabilized in PBS containing 0.5% Triton X-100 for 5 minutes. The sections were then washed three times with PBS and incubated in normal horse serum (1:30 ratio) for 30 minutes at room temperature. The sections were incubated with primary antibody (1:50 ratio) at 4°C overnight and at room temperature for 1 hour. The tissue sections were washed three times with PBS and incubated with secondary antibody (1:200 ratio) for 1 hour. After washing the section with PBS, the slides were mounted with Prolong Gold reagent (Invitrogen, Grand Island, NY, USA).

2.2.4 Western blot

Whole-cell protein extracts were prepared form cells grown to a confluence of ~80%. The cells were scratched from the surface of the cell-culture dish and boiled in SDS/PAGE sample buffer. The samples were analyzed by western blotting using antibodies against TOM20, TFAM, and β–actin.

2.2.5 Image analysis

For improving the S/N ratio of STED images and the accuracy of quantitative analysis, raw STED images were deconvoluted by *Imspector* and *Huygens*. The STED images were quantitatively analyzed by ImageJ software. The type of images was converted from RGB color to 8 bit and the images were adjusted by the factors such as band pass filter (FFT) and threshold. Average TOM20 cluster size, TOM20 cluster density, and average number of TFAM per a cell were measured from the STED images.

2.2.6 Immunogold stained EM sample preparation

Sub-cultured fibroblasts plated on 100 π dishes were exposed by UVB. Harvested cells at indicated time point were fixed with 4% paraformaldehyde

in pH 7.4 PBS buffer for 1 hour. The pellet was infiltrated into high concentration of sucrose and it was frozen in liquid nitrogen. Sectioning was performed by Cryo-ultramicrotome at -100°C. Before the immunogold staining, the sections were tested by immunofluorescence staining to confirm that the antigens on the section work normally. Immunogold labeling process was performed by incubating primary and 1 nm gold conjugated secondary antibodies. Silver enhancement was performed using the HQ silver enhancement kit (Nanoprobs, Stony Brook, NY, USA) for 3 minutes to make the gold nanoparticles larger than 10 nm by seed growth approach. Images were taken using TEM (JEM series, JEOL, Tokyo, Japan).

2.3 Results & Discussion

UVB irradiation induces mitochondrial fragmentation in skin primary fibroblast. Photoaging is an aging process induced by chronic UV exposure. UV induced extracellular matrix damage, which caused mainly by increased matrix metalloproteinase (MMP-1) and decreased collagen, plays a critical role in photoaging process. In our in vitro experiment, UV irradiation decreases protein level of procollagen and increases MMP-1 depending on irradiation power and elapsed time (Figure 2). Consequentially, it can induce skinfolds which is related with aging.

Previous study has shown that the apoptotic stimuli such as UV irradiation triggered the change of the mitochondrial matrix and brought about the release of cytochrome c[24]. The activity of mitochondria could be also adapted to changing cellular conditions: It has been suggested that short-term variations in energy demand may be compensated without modification of the mitochondrial enzyme contents, but modulation of the mitochondrial protein content has been observed during long-term adaptations[18,25].

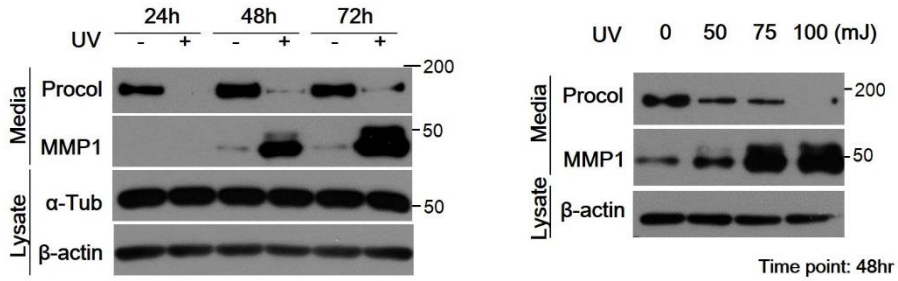

Figure 2. Western blots showing procollagen and MMP-1 protein levels in primary skin fibroblast after UV irradiation depending on (left) the elapse time after UV irradiation and (right) UV power. An antiserum against β-actin was used as a loading control.

Thus we tried to observe the change of mitochondrial structure under UV irradiation for studying correlation between UV irradiation and aging. When the cells were irradiated with increasing doses of UV, the PARP-1 enzymes involved in the repair process of damaged DNA changed the structure to cleaved form by activated caspases and the fragmented ratio of mitochondria from filamentous shape to spherical shape was increased. The truncation deactivates the enzyme and could induce to DNA fragmentation and cell apoptosis. Therefore cleaved form PARP-1 is regarded as a hallmark of apoptosis[26] (Figure 3).

At 30 minutes after 100 mJ/cm^2 UV treatment, the length variation of mitochondria were generally decreased without cell death while the cells by UV irradiation over 200 mJ/cm^2 cause both the morphological change of mitochondria and cell apoptosis (Figure 3 and 4). We visualized mitochondria stained with MitoTracker Deep Red FM, which is a membrane potential sensitive fluorescence dye, by confocal microscopy to compare mitochondrial activity of the sample fixed at two time points. As shown in Figure 5, UV irradiation significantly induced mitochondrial membrane potential difference in our case.

Using STED, we can analyze the distribution of TOM20 on mitochondrial outer membrane qualitatively and quantitatively. The central entry gate for almost all nuclear-encoded mitochondrial proteins is the TOM complex[18,27-29]. TOM20 is the initial recognition site for preproteins with presequences[30,31] on the mitochondrial outer membrane to allow movement of proteins and transfer the preproteins to the central receptor, TOM22[32,33]. Confocal microscopy provides overall morphology of homogeneously anti-TOM20 stained mitochondrial membrane within diffraction limit (Figure 6). Both the mitochondria labeled with anti-TOM20

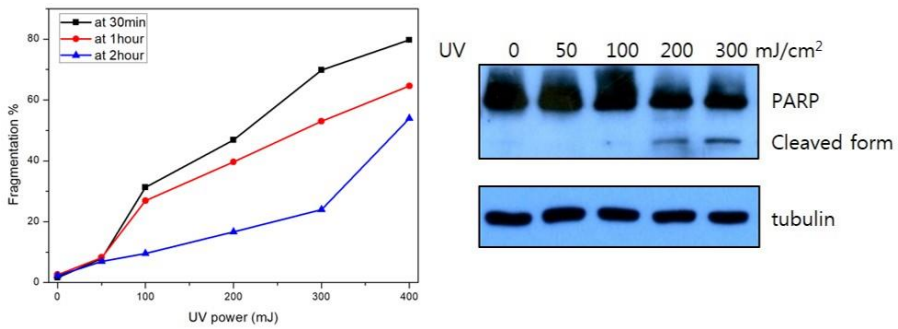

Figure 3. Correlation between UV expose, mitochondrial fragmentation, and cell apoptosis. (left) The ratio between the cell having fragmented mitochondria and total cells depending on UV power. (right) Western blot showing PARP protein levels after UV irradiation.

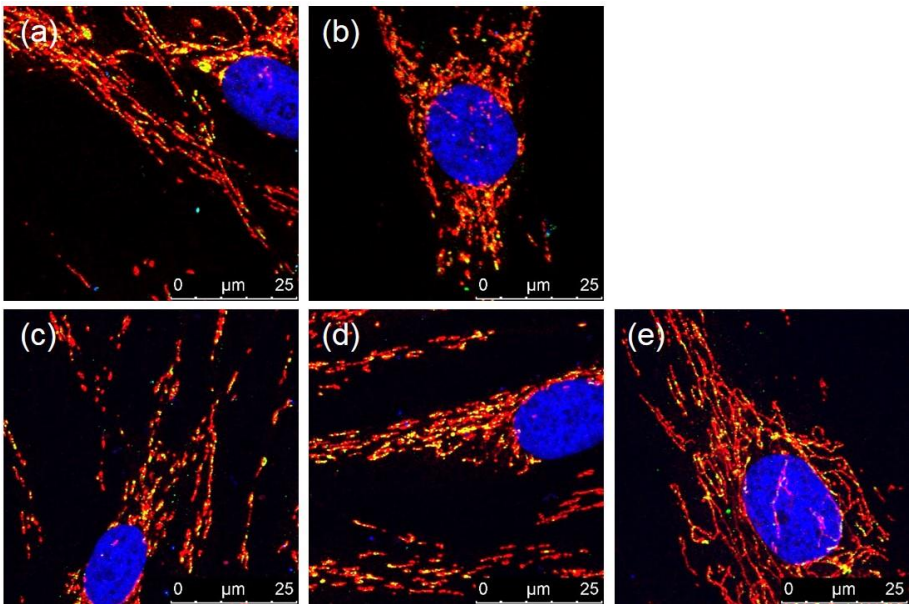

Figure 4. Confocal images for mitochondrial structure in primary skin fibroblast depending on the elapsed time after 100 mJ/cm^2 UV irradiation: (a) control, (b) 30 minutes, (c) 1 hours, (d) 2 hours, and (e) 24 hours. Color information: (red) TOM20, (yellow) TFAM, (blue) nuclei.

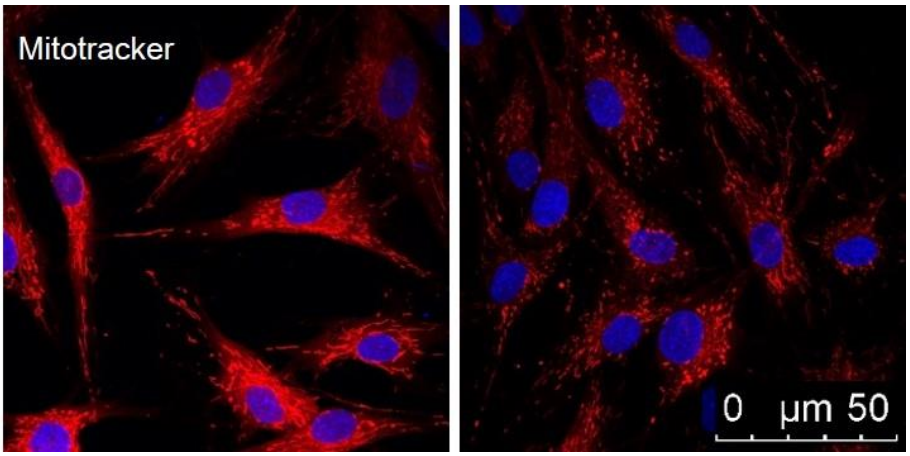

Figure 5. Confocal images treated by 200 nM Mitotracker: (left) control and (right) UV exposed cell (at 30 minutes).

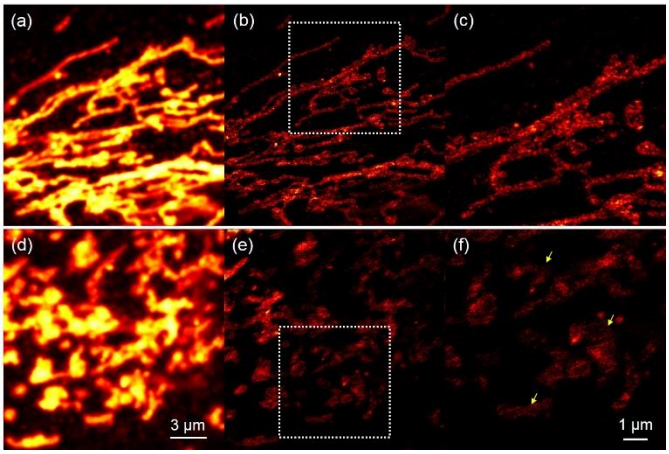

Figure 6. Comparison of TOM20 distribution between two groups. (Top) mitochondria in control fibroblasts: (a) confocal image, (b) STED image, and (c) x2 magnified STED image. (Bottom) mitochondria in UV exposed fibroblasts: (d) confocal image, (e) STED image, and (f) x2 magnified STED image.

and the mitochondria stained with MitoTracker usually appear to be interconnected tubular structure. Contrary to the images with conventional diffraction-limited fluorescence microscopy, STED nanoscopy enables to visualize that the TOM20 complexes exist cluster form (Figure 6).

We analyzed representative STED images of TOM20 clusters in two groups of fibroblast cells. The average diameter of TOM20 clusters was ~100 nm (Figure 7). Because the clusters were decorated by the primary and secondary antibodies and the unit pixel size were 50 nm, the clusters exhibit larger than the actual size. The broadness of the size distribution for TOM20 clusters were similar regardless of UV exposure. However, the density distribution of TOM20 clusters on mitochondria significantly differed among two groups (Figure 8). Particularly, the cluster density relatively decreased by UVB treatment and the clusters in UV exposed fibroblasts were localized at the rim of mitochondrial outer membrane. These suggest that we can observe nanoscale distribution of TOM20 clusters and distinguish quantitatively the cluster density difference due to the acute aging related stimulation using super-resolution STED nanoscopy. In the previous study by Hell group, they reported that the nanoscale distribution of the TOM20 clusters might differ because of different functional requirements of mitochondria[18].

To validate the analytical method based on fluorescence imaging, we performed TEM measurement using immunogold staining for normal mitochondria and fragmented mitochondria on the sections chopped by cryo-ultramicrotome (Figure 9). We found that the distribution patterns from TEM imaging agree very well with our STED measurement. Compared with STED, TEM requires complicated sample preparation and can also easily damage the field of view including the mitochondrial membrane and even immuno-stained gold beads due to the high voltage electron. Moreover, TEM images

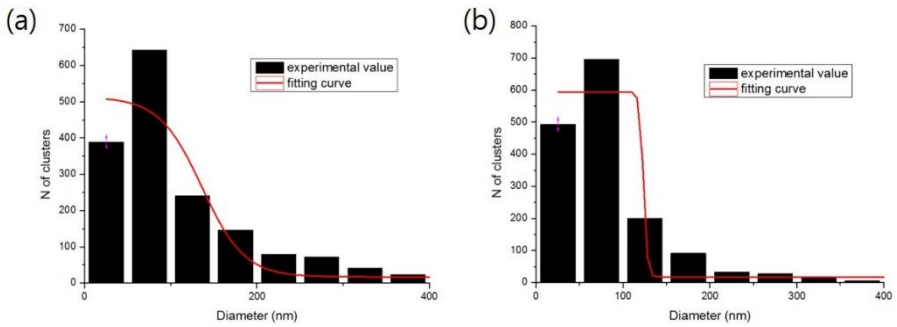

Figure 7. Analysis of the diameter of TOM20 clusters: (a) control (b) UV exposed cell (at 30 minutes).

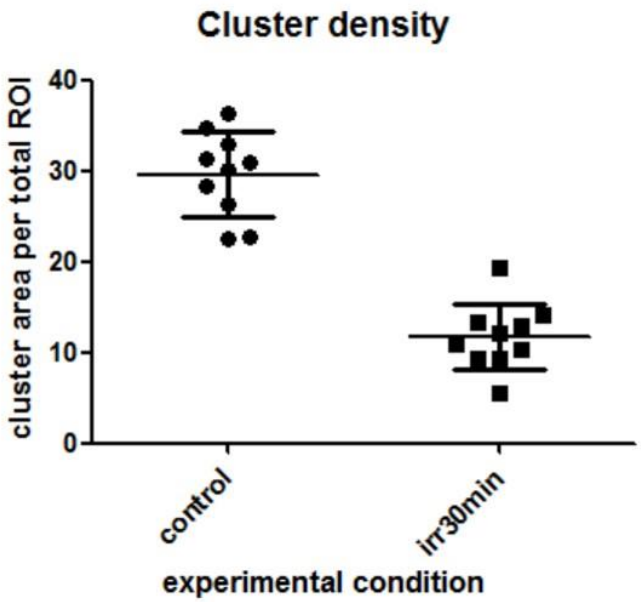

Figure 8. The analysis of TOM20 cluster density in mitochondria. At least 10 ROI areas were quantified per a sample. $p<0.05$ compared with control using t-test.

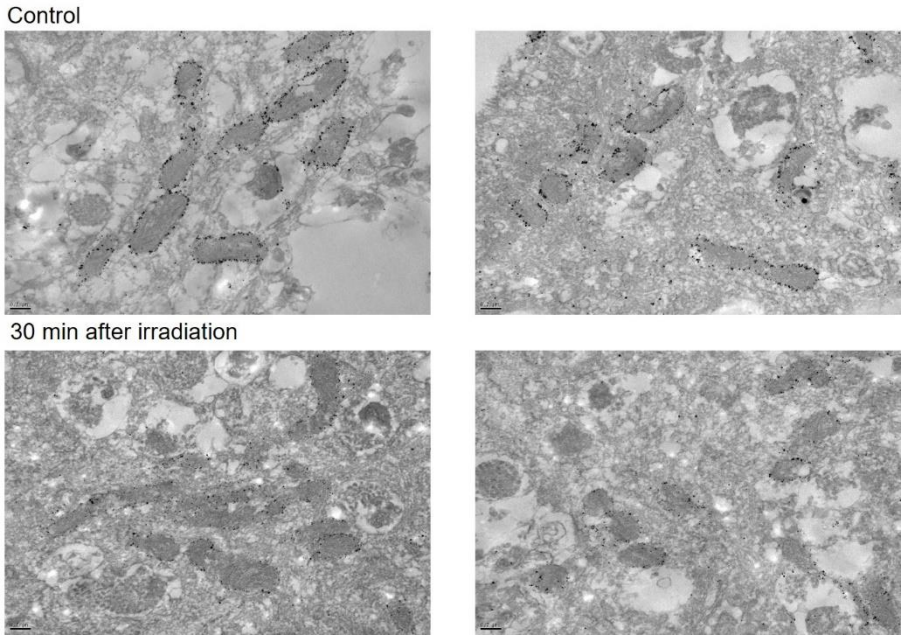

Figure 9. Transmission electron microscopy micrographs using immunogold staining methods for TOM20: (top) control, (bottom) UV exposed cell (at 30 minutes). Scale bar: 200 nm.

from the immunogold stained section only present the TOM20 clusters on the very narrow cutting plane, not for 3 dimensional structure of mitochondrial outer membrane.

In a single cell level, TFAM, related with aging, can be analyzed quantitatively by STED nanoscopy. TFAM is the main protein component of nucleoids and has several functions: it mainly help to pack and retain mtDNA in mammalian cells, and is involved in mitochondrial transcription and replication. TFAM has the ability to bind, wrap, bend, and unwind DNA regardless of sequence-specificity, which is similar to the motion of other HMG box proteins[34,35]. Mitochondrial DNA loss and embryonic lethality occur in TFAM gene knockout mouse [36,37]. As a core element for the mitochondrial transcription, TFAM is necessary to gather the transcription machinery for initiation process of transcription[38]. TFAM also could contribute to mtDNA replication since the initiation is related with an RNA primer synthesized by the transcription from light strand promoter (LSP). Importantly, TFAM, recognized a key activator of mitochondrial transcription and a main component of nucleoid structure, has significantly age-associated expression changes in genes[39].

Confocal imaging of mitochondrial nucleoids labeled by TFAM antibodies shows sparsely populated pattern and indiscerptible TFAM location on the mitochondrial network of skin primary fibroblast (Figure 10). The nucleoids closely located within diffraction limit seem to be one particle in the confocal images because the actual size of nucleoids is below ~250 nm. To measure the size of nucleoids and the distribution precisely, we used STED nanoscopy. The nucleoid determined by STED nanoscopy had smaller size than the one proposed by confocal microscopy. We could resolve individual nucleoid using STED nanoscopy (Figure 10). Most of them had an ellipsoid that is

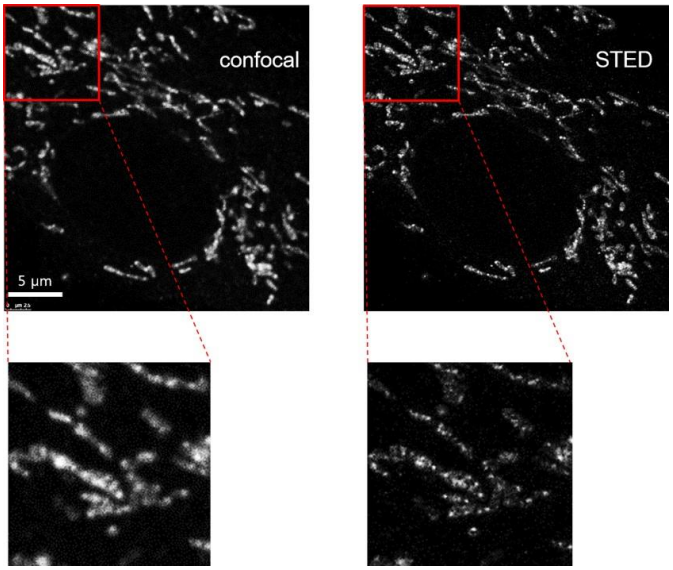

Figure 10. TFAM images observed by (left) confocal and (right) STED. Scale bar: 5 µm.

close to spherical shape. The average diameter of nucleoid was ~100 nm which is similar with the actual size of antibody labeled nucleoids. Besides, this value approximated a mean size of mitochondrial nucleoids of ~110 nm in mouse fibroblast which was presented by PALM to identify expression of a fluorescent mEos2-tagged TFAM protein in transfected cells, or and dSTORM to detect mtDNA with anti-bodies[36,40]. This result means that super-resolution microscopy can investigate that mitochondrial nucleoids in mammalian cell have a uniform size[34].

Since TFAM closely connected to aging, we quantitative analyzed the nucleoids per cell in the fibroblast cells. The average number of nucleoids, labeled by an antibody against TFAM, observed by STED nanoscopy is ~1.5 times larger than that of nucleoids observed by confocal microscopy (Figure 11). Next, we compared average nucleoids depending on the elapsed time after acute UV irradiation. By using STED nanoscopy, we found that the average nucleoids were transiently changed by UV irradiation (Figure 12).

In Figure 13, overlay images suggest that TFAM has different distribution tendency depending on the experimental condition. Nucleoids of mitochondria in normal cells were dispersed linearly such as tubular structure. But nucleoids in fragmented mitochondria by UV irradiation are spread randomly.

On paraffin embedded Tissue, mitochondrial translocase proteins can be analyzed quantitatively using STED. Confocal microscopy demonstrated the strong expression of TOM20 in all mouse skin tissues whereas the antibody against TFAM did not operated (Figure 14). Also the blue signal from DAPI to highlight nuclei was detected both in all tissues. We confirmed that multicolor fluorescence imaging was feasible on paraffin embedded tissue and mitochondrial proteins were observed on 3 parts of the tissues

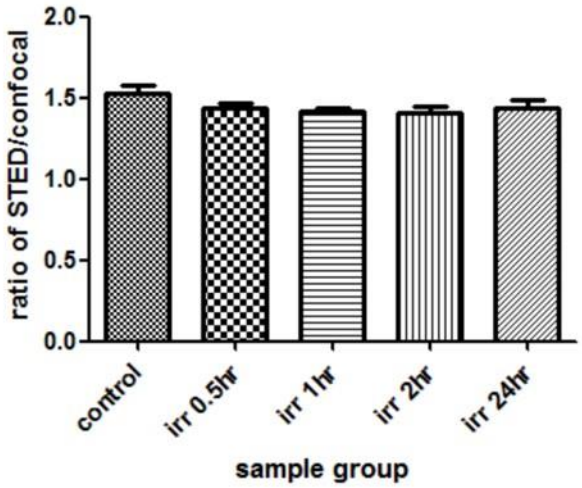

Figure 11. Ratio of the number of TFAMs measured by STED nanoscopy vs. the number of TFAMs measured by confocal microscopy. Nucleoids were labeled by TFAM antibody.

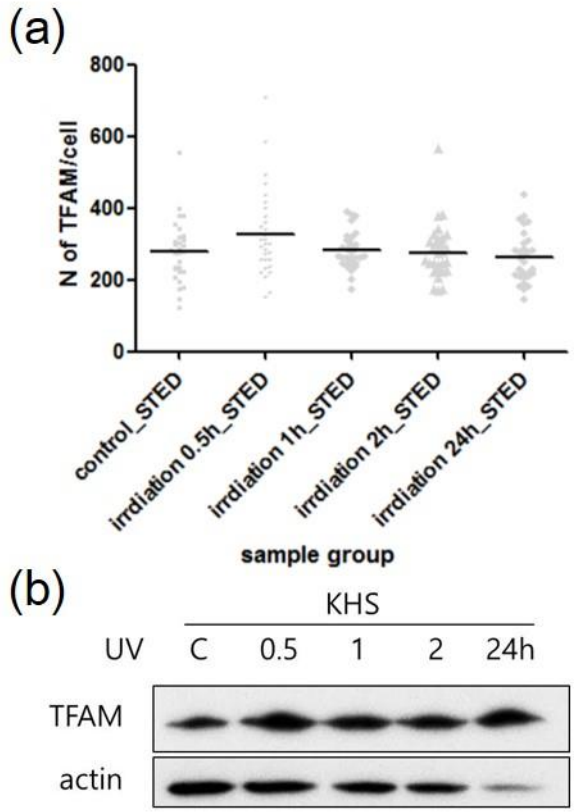

Figure 12. Analysis of the number of TFAM at each time point: (a) TFAM in STED images were quantitative measured by ImageJ software. (b) Western blot were showing TFAM protein levels.

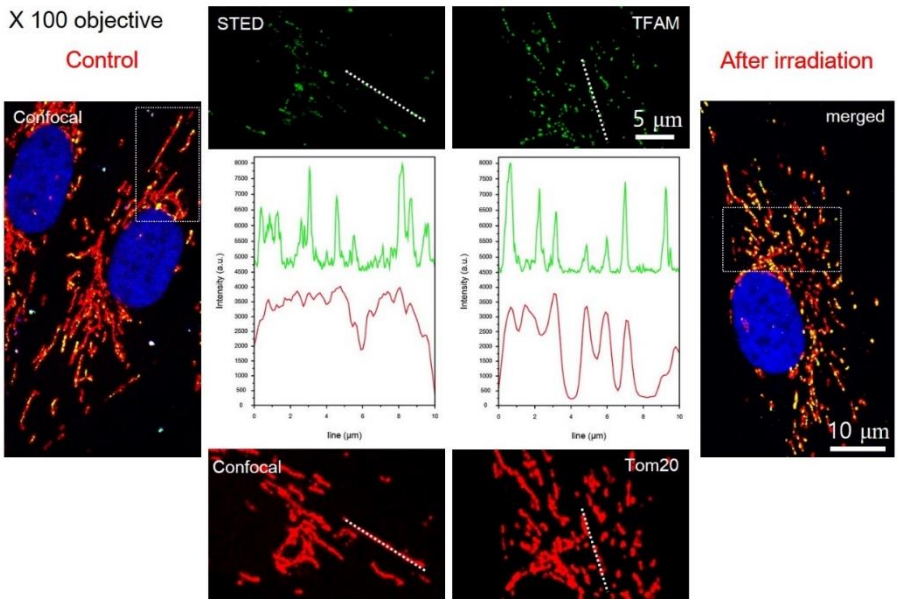

Figure 13. TOM20 morphology and TFAM distribution tendency in fibroblast: (left) control and (right) UV exposed cell (at 30 minutes). Color information: (red) TOM20, (yellow and green) TFAM, (blue) nuclei.

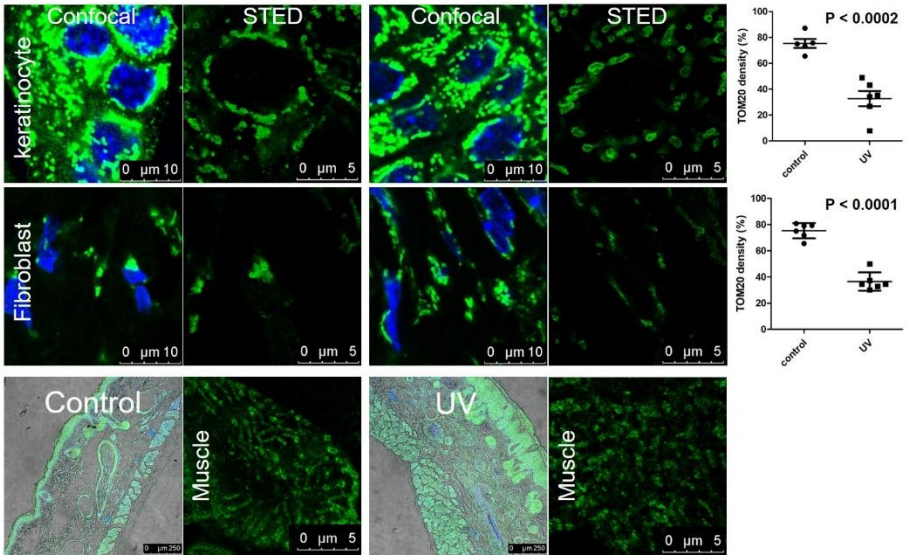

Figure 14. UV induced change of mitochondria in mouse skin tissue. Cluster density analysis: (top) for keratinocyte, (middle) fibroblast, (bottom) dermal tissue and muscle in the tissue.

consisting of keratinocyte, fibroblast, and muscle.

We investigated the feasibility of visualizing the nanoscale distribution of TOM20 using STED nanoscopy in tissues. In enlarged STED image, TOM20 had spherical cluster shape within mitochondria. This mitochondrial distribution pattern was fully comparable to the result observed in cultivated skin primary fibroblast. These data suggested that the paraffin embedded tissue had structural preservation on the nanoscale.

TOM20 clusters were evenly spread on mitochondria of keratinocytes in normal mouse skin tissues while the small amount of TOM20 were observed in chronic UV exposed mouse tissues. Similar tendency were appeared on the fibroblasts in two types of tissues. We also analyzed the distribution of TOM20 clusters quantitatively. Contrary to the TOM20 clusters already mentioned, the clusters on the muscles had different pattern. Linearly arranged TOM20 clusters had shorten by chronic UV irradiation. We concluded that STED super-resolution microscopy was suited to analyze nanoscale distribution of aging related proteins in tissues preserved by standard storage method.

2.4 Conclusion

Photoaging describes distinct clinical and functional features of chronically sun-exposed dermis. Although it has been studied for some time, its molecular mechanisms have been recently discovered by the advanced macroscopic and microscopic technology. The investigation for pathophysiological mechanisms of photoaging might suggest the standard for evaluating the effectiveness of photoprotective substances and contribute to the establishment of new strategies which will provide the functions such as protection and repair of photodamaged human dermis[41]. Because

mitochondrial nanoscale morphology is a critical readout of cell internal state, there is a need to develop assays and tools relevant for the screening of mitoprotective agents in skin originated cell type repeatedly exposed to high dose of UV radiation[42].

We demonstrated the potential of STED nanoscopy to evaluate the aging degree as an analysis tool. In sub cultured fibroblast, conventional confocal microscopy provided overall mitochondrial membrane structure and TFAMs located in area within diffraction limit as one particle. However, using super-resolution STED nanoscopy, we could resolve individual translocase of mitochondria and perform more accurate quantitative analysis of TFAM. In addition, it was possible to distinguish the distribution of mitochondrial translocases between normal tissues and chronic UV exposed tissue. Our results suggested that highly resolved fluorescence imaging was very useful for quantitative analysis of TFAM and mitochondrial translocase activity.

Developing this method to universal technology for evaluating biological aging will need further improvements in automated super-resolution imaging system and in image analysis algorithm for counting the number of molecules and evaluating the heterogeneity of the protein distribution[43]. Nanoscale biological microscopy with genetically encoded markers can implement quantitative assay of aging-related proteins in living cells[44].

2.5 Reference

1. Rafelski, S. M. Mitochondrial network morphology: building an integrative, geometrical view. *BMC Biol* **11**, 71 (2013).

2. Jayashankar, V. & Rafelski, S. M. Integrating mitochondrial organization and dynamics with cellular architecture. *Curr Opin Cell Biol* **26**, 34-40 (2014).

3. Friedman, J. R. & Nunnari, J. Mitochondrial form and function. *Nature* **505**,

335-343 (2014).

4. Nunnari, J. & Suomalainen, A. Mitochondria: in sickness and in health. *Cell* **148**, 1145-1159 (2012).

5. Schmidt, R. *et al.* Mitochondrial cristae revealed with focused light. *Nano Lett* **9**, 2508-2510 (2009).

6. Frey, T. G. & Mannella, C. A. The internal structure of mitochondria. *Trends Biochem Sci* **25**, 319-324 (2000).

7. Bowman, A. & Birch-Machin, M. A. Age-Dependent Decrease of Mitochondrial Complex II Activity in Human Skin Fibroblasts. *J Invest Dermatol* **136**, 912-919 (2016).

8. Peterson, C. M., Johannsen, D. L. & Ravussin, E. Skeletal muscle mitochondria and aging: a review. *J Aging Res* **2012**, 194821 (2012).

9. Youle, R. J. & van der Bliek, A. M. Mitochondrial fission, fusion, and stress. *Science* **337**, 1062-1065 (2012).

10. Passos, J. F., von Zglinicki, T. & Saretzki, G. Mitochondrial dysfunction and cell senescence: cause or consequence? *Rejuvenation Res* **9**, 64-68 (2006).

11. Berneburg, M. *et al.* Singlet oxygen mediates the UVA-induced generation of the photoaging-associated mitochondrial common deletion. *J Biol Chem* **274**, 15345-15349 (1999).

12. Chen, J. H. *et al.* Loss of proliferative capacity and induction of senescence in oxidatively stressed human fibroblasts. *J Biol Chem* **279**, 49439-49446 (2004).

13. Hauser, D. N. & Hastings, T. G. Mitochondrial dysfunction and oxidative stress in Parkinson's disease and monogenic parkinsonism. *Neurobiol Dis* **51**, 35-42 (2013).

14. Chen, Q. & Ames, B. N. Senescence-like growth arrest induced by hydrogen peroxide in human diploid fibroblast F65 cells. *Proc Natl Acad Sci*

U S A **91**, 4130-4134 (1994).

15. Chen, Q. M. *et al.* Molecular analysis of H2O2-induced senescent-like growth arrest in normal human fibroblasts: p53 and Rb control G(1) arrest but not cell replication. *Biochem J* **332**, 43-50 (1998).

16. Chen, Q. M., Tu, V. C. & Liu, J. P. Measurements of hydrogen peroxide induced premature senescence: Senescence-associated beta-galactosidase and DNA synthesis index in human diploid fibroblasts with down-regulated p53 or Rb. *Biogerontology* **1**, 335-339 (2000).

17. Revelo, N. H. & Rizzoli, S. O. *Advanced Fluorescence Microscopy: Methods and Protocols, Methods in Molecular Biology*. Vol. 1251 12 (2015).

18. Wurm, C. A. *et al.* Nanoscale distribution of mitochondrial import receptor Tom20 is adjusted to cellular conditions and exhibits an inner-cellular gradient. *P Natl Acad Sci USA* **108**, 13546-13551 (2011).

19. Born, M. & Wolf, E. *Principles of Optics*. 7th Ed. edn, (Cambridge Univ Press, Cambridge, 2002).

20. Huang, B., Jones, S. A., Brandenburg, B. & Zhuang, X. W. Whole-cell 3D STORM reveals interactions between cellular structures with nanometer-scale resolution. *Nat Methods* **5**, 1047-1052 (2008).

21. Jans, D. C. *et al.* STED super-resolution microscopy reveals an array of MINOS clusters along human mitochondria. *P Natl Acad Sci USA* **110**, 8936-8941 (2013).

22 .Singh, H. *et al.* Visualization and quantification of cardiac mitochondrial protein clusters with STED microscopy. *Mitochondrion* **12**, 230-236 (2012).

23 .Ilgen, P. *et al.* STED Super-Resolution Microscopy of Clinical Paraffin-Embedded Human Rectal Cancer Tissue. *Plos One* **9** (2014).

24. Gao, W. H., Pu, Y. M., Luo, K. Q. & Chang, D. C. Temporal relationship between cytochrome c release and mitochondrial swelling during UV-induced

apoptosis in living HeLa cells. *J Cell Sci* **114**, 2855-2862 (2001).

25. Devin, A. & Rigoulet, M. Mechanisms of mitochondrial response to variations in energy demand in eukaryotic cells. *Am J Physiol-Cell Ph* **292**, C52-C58 (2007).

26. Soldani, C. & Scovassi, A. I. Poly(ADP-ribose) polymerase-1 cleavage during apoptosis: An update. *Apoptosis* **7**, 321-328 (2002).

27. Hoogenraad, N. J., Ward, L. A. & Ryan, M. T. Import and assembly of proteins into mitochondria of mammalian cells. *Bba-Mol Cell Res* **1592**, 97-105 (2002).

28. Neupert, W. & Herrmann, J. M. Translocation of proteins into mitochondria. *Annu Rev Biochem* **76**, 723-749 (2007).

29. Chacinska, A., Koehler, C. M., Milenkovic, D., Lithgow, T. & Pfanner, N. Importing Mitochondrial Proteins: Machineries and Mechanisms. *Cell* **138**, 628-644 (2009).

30. Sollner, T., Griffiths, G., Pfaller, R., Pfanner, N. & Neupert, W. Mom19, an Import Receptor for Mitochondrial Precursor Proteins. *Cell* **59**, 1061-1070 (1989).

31. Saitoh, T. *et al.* Tom20 recognizes mitochondrial presequences through dynamic equilibrium among multiple bound states. *Embo J* **26**, 4777-4787 (2007).

32. Kiebler, M. *et al.* The Mitochondrial Receptor Complex - a Central Role of Mom22 in Mediating Preprotein Transfer from Receptors to the General Insertion Pore. *Cell* **74**, 483-492 (1993).

33. Van Wilpe, S. *et al.* Tom22 is a multifunctional organizer of the mitochondrial preprotein translocase. *Nature* **401**, 485-489 (1999).

34. Kukat, C. *et al.* Super-resolution microscopy reveals that mammalian mitochondrial nucleoids have a uniform size and frequently contain a single

copy of mtDNA. *P Natl Acad Sci USA* **108**, 13534-13539 (2011).

35. Fisher, R. P., Lisowsky, T., Parisi, M. A. & Clayton, D. A. DNA Wrapping and Bending by a Mitochondrial High Mobility Group-Like Transcriptional Activator Protein. *J Biol Chem* **267**, 3358-3367 (1992).

36. Kukat, C. & Larsson, N. G. mtDNA makes a U-turn for the mitochondrial nucleoid. *Trends Cell Biol* **23**, 457-463 (2013).

37. Larsson, N. G. *et al.* Mitochondrial transcription factor A is necessary for mtDNA maintenance and embryogenesis in mice. *Nat Genet* **18**, 231-236 (1998).

38. Shi, Y. H. *et al.* Mammalian transcription factor A is a core component of the mitochondrial transcription machinery. *P Natl Acad Sci USA* **109**, 16510-16515 (2012).

39. Kalfalah, F. *et al.* Inadequate mito-biogenesis in primary dermal fibroblasts from old humans is associated with impairment of PGC1A-independent stimulation. *Exp Gerontol* **56**, 59-68 (2014).

40. Brown, T. A. *et al.* Superresolution Fluorescence Imaging of Mitochondrial Nucleoids Reveals Their Spatial Range, Limits, and Membrane Interaction. *Mol Cell Biol* **31**, 4994-5010 (2011).

41. Berneburg, M., Plettenberg, H. & Krutmann, J. Photoaging of human skin. *Photodermatol Photo* **16**, 239-244 (2000).

42. Juge, R. *et al.* Quantification and Characterization of UVB-Induced Mitochondrial Fragmentation in Normal Primary Human Keratinocytes. *Sci Rep-Uk* **6**, 35065 (2016).

43. Jakobs, S. & Wurm, C. A. Super-resolution microscopy of mitochondria. *Curr Opin Chem Biol* **20**, 9-15 (2014).

44. Willig, K. I. *et al.* Nanoscale resolution in GFP-based microscopy. *Nat Methods* **3**, 721-723 (2006).

Chapter 3. Highly Fluorescence Water Soluble Turn-on Diarylethene for Super-resolution Bioimaging over a Broad pH Range

[This chapter was published in Dyes and Pigments, 158, 36-41 (2018).]

3.1 Introduction

Recent advances in the far-field fluorescence microscopy have allowed us to investigate cellular structure and dynamics with low sample damage but high imaging contrast.[1-2] Particularly, super-resolution microscopy is drawing much attention because it is able to reveal sub-nanostructure of soft-matter materials and biological samples at a single molecule level.[3-4] In the super-resolution microscopy, the photophysical and chemical properties of photoswitchable fluorophore used as an imaging probe are one of the key factors that decide quality of the imaging.[5] However, conventional imaging probes for the super-resolution microscopy have intrinsic limitations. For example, cyanine dyes have low chemical stability. Photoswitchable fluorescent proteins are difficult to trace cell dynamics and have limited resolution due to their big size.[6-9]

On the other hand, diarylethenes (DAEs) have high thermal stability, reversibility, fatigue resistance, and fast switching rate, making them an ideal candidate for the super-resolution imaging.[10-14] Particularly, the turn-on type DAEs have been successfully applied for the PALM-based super-resolution microscopy to reveal soft-matter structures with an advantage of high fluorescence on/off contrast.[15-16] Very recently, Hell group reported water-soluble DAEs bearing multiple carboxylic acid groups and applied them for super-resolved bioimaging based on RESOLFT and STORM technique.[17] Although the DAEs with carboxylic acids showed suitable fluorescence modulation and enough solubility in aqueous buffers at physiological pH, high pKa value of the carboxylic acid group (pKa ~ 4.2)[18] prevents their direct application in various biological environments particularly below pH 5, such as in lysosomes, in tumor cells, and in some micro-organisms (e.g., eukaryotic cells and enteric pathogen) that can experience highly acidic conditions.[19]

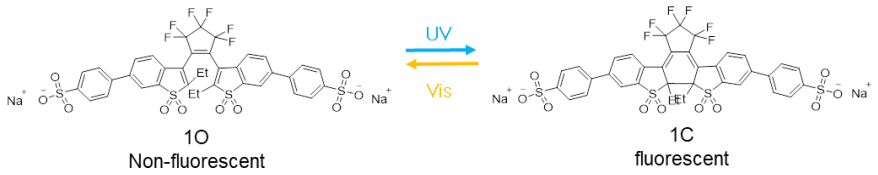

Scheme 1. Chemical structure and photochromic reaction scheme between open (**1O**) and closed (**1C**) form of SO3-BPDBTEO (**1**).

Therefore, developing a DAE, which is highly soluble and applicable as a super-resolution imaging probe over a broad pH range, is highly desirable and indispensable.[20-21]

Herein we present a water-soluble turn-on type DAE that can be used as a probe in PALM-based super-resolution microscopy for imaging biological samples at various pH conditions. To this end, we prepared SO3-BPDBTEO (**1**) bearing two sodium sulfonate groups, whose pKa value (pKa ~ −2.8) is significantly lower than that of the carboxylate group,[18] in the phenyl ring at C6,6′-position of 1,2-bis(2-ethyl-6-phenyl-1-benzothiophen-1,1-dioxide-3-yl)perfluorocyclopentene core (see Scheme 1). The details of synthesis procedure for **1** have been reported elsewhere.[22-23] The chemical structure of **1** is fully characterized by ^{1}H NMR, ^{13}C NMR, 2D NMR (HSQC), and MALDI-TOF (I excepted these data for this dissertation).

3.2 Experimental Method

3.2.1 Cell preparation for imaging

HeLa cells were grown on the bottom of a cover glass-bottom dish (SPL Life sciences, 100350) in Dulbecco's Modified Eagle's Medium (DMEM) with 10% FBS at 37 °C and 5% CO_2 concentration. After we removed the medium, the cells were incubated with 50 μM SO3-BPDBTEO added DMEM for 24 hours. The cells on the dish were washed with PBS and fixed in 4% paraformaldehyde in PBS. For confocal imaging, we filled up the dish with PBS.

3.2.2 Trypan blue exclusion for cell viability

The viability test of HeLa cells was examined by trypan blue exclusion assay referring to reference.[6] HeLa cells were seeded into 6-well plates at 2×10^{4} per

a well. After the cells were grown for 24 hours at 37℃ under 5% CO_2, SO3-BPDBTEO at concentrations of 2, 10, 20, 50, 70 μM was added to each well and incubated for 24 hours under the identical cell culture condition. After then, they were washed with 1x PBS three times and collected by trypsinization. The collected cells were centrifuged and suspended with 0.4% trypan blue solution. We counted the unstained and stained cells separately using hemocytometer and calculated the percentage of viable cells as follows.[3]

$$viable\ cells\ (\%) = \frac{total\ No\ of\ viable\ cells\ per\ mL\ of\ aliquot}{total\ No\ of\ cells\ per\ mL\ of\ aliquot} \times 100$$

3.2.3 Confocal fluorescence imaging

Confocal Microscope (TCS SP8 X, Leica) was used with a HCX PL APO CS 10x/0.40 dry objective and a HC PL APO CS2 63x/1.40 oil immersion objective. To turn on the fluorescence, a 365 nm light source from a UV lamp was irradiated for 3 minutes at a distance of 5 cm from the sample. To turn off the fluorescence, a 458 nm argon laser was exposed to 100% intensity for 5 minutes. The 50% power of 458 nm excitation source from Argon were used for fluorescence imaging. The fluorescence detection range from 499 nm to 610 nm were established by prism dispersion based spectral detector. All of images were optically magnified twice by LAS X software.

3.2.4 Super-resolution fluorescence imaging

Localization based super-resolution imaging was carried out using commercially available ELYRA P.1 instrument by Zeiss with 100x 1.46 NA oil-immersion objective. A 488 nm excitation source was used for fluorescence imaging. The fluorescence signal was separated from excitation

laser by a 495-590 nm bandpass filter and detected using EMCCD camera at 295K resulting in an image with 100 nm per pixel. 15000 frames of image were acquired for one movie.

The obtained movie was analyzed to reconstruct wide field image and super-resolution image with PALM plugin for Zen black software. The wide field image was generated as the sum of all frames. For obtaining the best reasonable super-resolution image, the pixel resolution for super-resolution imaging was 10 nm per pixel and the spots having PSF width from 100 to 200 nm were analyzed to exclude the patterns by unreasonable parameters. Additionally, we rendered the super-resolution image by the factor such as localized precision ranging between 10 and 50 nm to separate the fluorescence signal at the single molecule level.

3.3 Results & Discussion

Absorption and emission spectra of **1** in open (**1O**) and closed form (**1C**) are shown in Figure 1. **1O** in aqueous solution has an absorption peak at 335 nm and exhibits no fluorescence. But, upon irradiation of UV-light, **1O** undergoes a cyclization reaction to form **1C**. In sharp contrast to the open form, **1C** has visible-light absorption peaking at 450 nm and exhibits strong yellow fluorescence ($\lambda_{em,max}$ = 526 nm) with a fluorescence quantum yield (Φ_F) of 0.45 and a fluorescence lifetime (τ) of 1.70 ns. Upon visible-light irradiation, yellow solution of **1C** turns back into the clear transparent solution to form its original **1O**. The quantum yield of cyclization ($\Phi_{O\rightarrow C}$) and cycloreversion ($\Phi_{C\rightarrow O}$) in the aqueous solution are determined to be 0.22 and 8.67×10^{-4},respectively. Because **1** has high fluorescence efficiency and low cycloreversion quantum yield ($\Phi_F/\Phi_{C\rightarrow O}$ = 519) in the aqueous solution, it is expected that **1** is a promising candidate for a bioimaging probe in coordinate-

stochastic super-resolution microscopy such as PALM.[24]

.

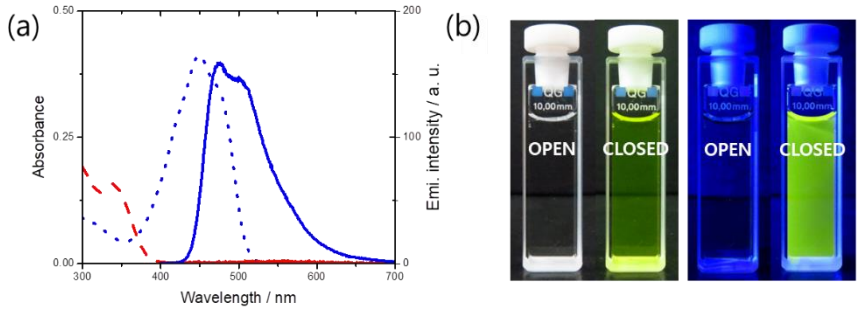

Figure 1. (a) Absorption (dashed lines) and emission (solid lines) spectra of the open form (**1O**, sky-blue lines) and the closed form (**1C**, blue lines). (b) Photographs of **1O** and **1C** in water ($c = 1 \times 10^{-5}$M) under room light (left) and UV light (right).

To test reversibility of the photochromic reaction between **1O** and **1C**, fluorescence spectra of **1** in water were monitored upon repetitive irradiation of UV and visible-light. To our surprise, for 20 photoswitching cycles, the fluorescence of the solution is almost perfectly modulated between on and off, and **1C** shows only 6% intensity decrease in the on state (Figure 2a). It means that **1** has high reversibility and fatigue resistance to the light stimuli in the aqueous condition

Most interestingly, the photoswitching ability of **1** is hardly affected by pH changes of the solution between 3 and 10 (Figure 2b). It is found that the relative Φ_F of **1C** is consistently maintained in KCl buffer solution at various pH without any aggregation and absorption color changes.

To evaluate bioimaging utilities of **1** in cells, sub-cultured HeLa cells were stained with **1** by the methods reported in the literature.[25] The stained cells were exposed to 365 nm of UV light by a handheld UV lamp for 3 minutes to form **1C**. As expected, bright fluorescence is observed from the stained cells by confocal microscope, while the unstained cells exhibit no fluorescent signal even after UV irradiation (Figure S5).

It is noteworthy that the fluorescence of the stained HeLa cells is reversibly turned on and off by sequentially alternating exposures of UV and visible light to the cells (Figure 3a and 3b). Through this photoswitching probe method, the autofluorescence of the HeLa cells can be removed and thus high contrast images are obtained without special imaging buffers to suppress photobleaching and improve dye stability.

Encouraged by the successful fluorescence imaging of **1** in the HeLa cells, we applied **1** to monitor the cells at various pH condition. The results of microscopic analysis show that **1** maintains its photoswitching performance and fluorescence intensity in the cells irrespective of pH condition (Figure 3c

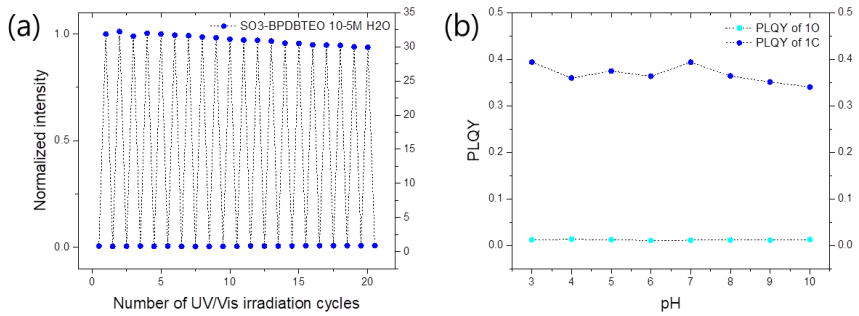

Figure 2. (a) Normalized fluorescence intensity change of **1** in water (c = 1×10^{-5} M) monitored at 430 nm upon alternating irradiation of UV and visible-light. Photoswitching is repeated for 20 cycles. (b) Fluorescence quantum yield variation of **1O** and **1C** in KCl buffer solution at various pH (c = 1×10^{-5}M).

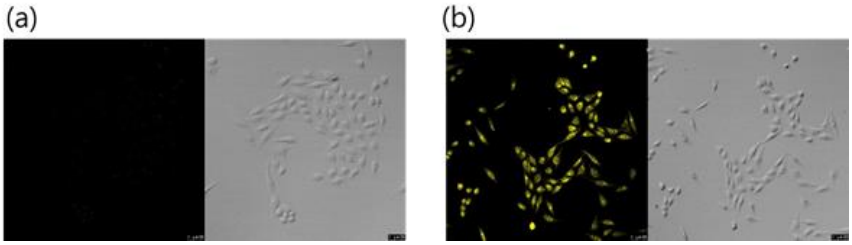

Figure S5. Confocal images of HeLa cells: fluorescent (left) and DIC (right) images at 488 nm. (a) Images of HeLa cells untreated. (b) Images of HeLa cells stained with 50 μM of **1**.

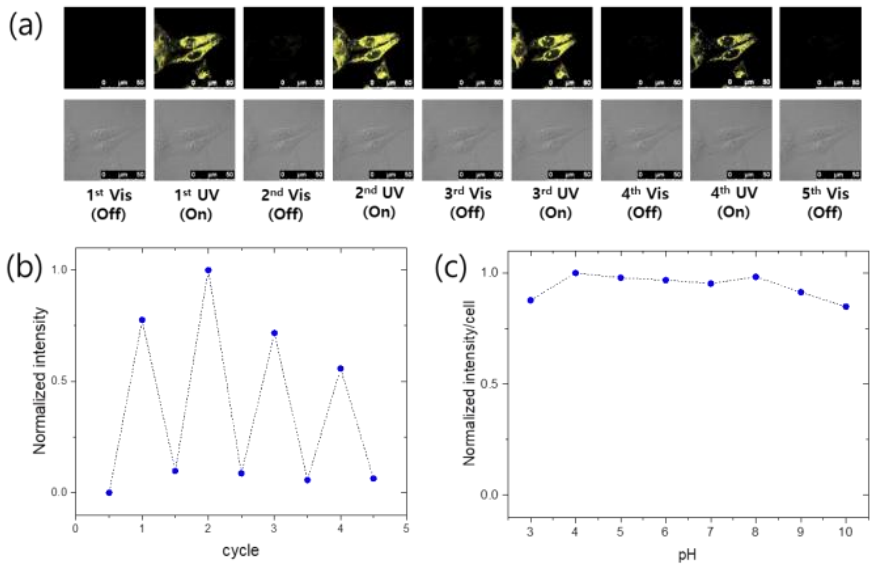

Figure 3. Photoswitching experiments performed on HeLa cell. (a) Confocal fluorescence microscope images of the HeLa cells stained with 1 in PBS (pH 7): fluorescence (top) and DIC (bottom) images obtained by repetitive irradiation of visible light (458nm, 5min) and UV (365, 3min). (b) Normalized fluorescence intensity measured from the HeLa cells during the photoswitching experiments. (c) Normalized fluorescence intensity of the HeLa cells stained with 1 at various pH of the mounting media after UV-light irradiation to form 1C.

and Figure S7 and S8). It well demonstrates the versatility of **1** for imaging in various biological conditions.

Although **1** shows promising photophysical properties for bioimaging in the cells, it is important to have low cytotoxicity for practical biological application as an imaging probe. To confirm the cytotoxic effect of the molecule, HeLa cells were treated with various concentration of **1** (2, 10, 20, 50, and 70 μM) for 24 h, and cell viability was monitored by the trypan blue exclusion assay. The treatment of **1** induces no morphological change of the cells and more than 95% of cells are viable, which means that the molecule has low cytotoxicity (Figure S6).

To verify the feasibility of **1** to super-resolution microscopy, we investigated intracellular diffusivity of **1**. We first irradiated the HeLa cells stained with **1** by UV light to turn on the fluorescence and then monitored the fluorescence of the cells for 30 min. It is observed that a line profile of the fluorescence intensity of the cells is virtually unchanged for 30 min (Figure S9). It indicates that most of the **1** molecules would stay in the region where they were firstly stained while acquiring the super-resolution images.[26] Based on these observations and the superior photoswitching properties of **1**, we attempted PALM-based super-resolution imaging of the HeLa cells. As shown in Figure 4, we could acquire an image that has a higher resolution than the wide-field image, which is enough to find the position of the **1** molecules with high accuracy in the cells.

3.4 Conclusion

In conclusion, a water-soluble turn-on type diaryethene **1** bearing sodium sulfonate groups is reported. It showed reversible photochemical transformation with fluorescence on/off switching by UV and visible light

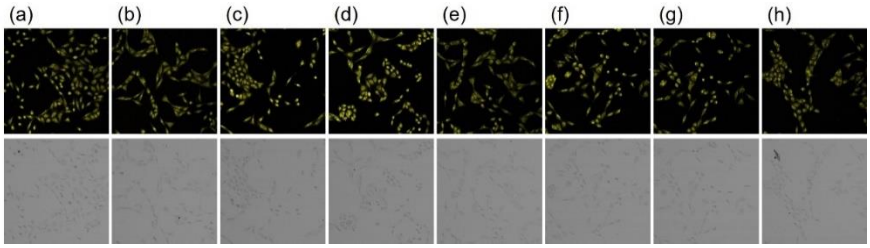

Figure S7. Confocal microscope images of HeLa cells with 50 μM of **1** at various pH. DIC (bottom) and fluorescent (top) images in PBS at (a) pH 3, (b) pH 4, (c) pH 5, (d) pH 6, (e) pH 7, (f) pH 8, (g) pH 9, and (h) pH 10.

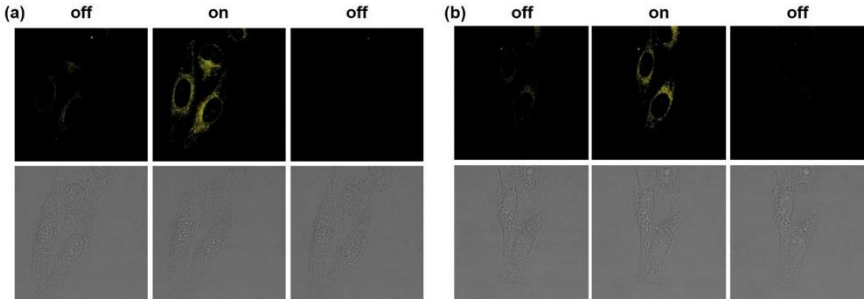

Figure S8. Photoswitching experiments performed on fixed HeLa cells stained with 50 μM of **1**. Confocal images for HeLa cells with DIC (bottom) and fluorescent (top) imaging obtained by repeated irradiation of UV (365, 3min) and visible light (458nm, 5min) (a) in pH 3 PBS and (b) in pH 10 PBS.

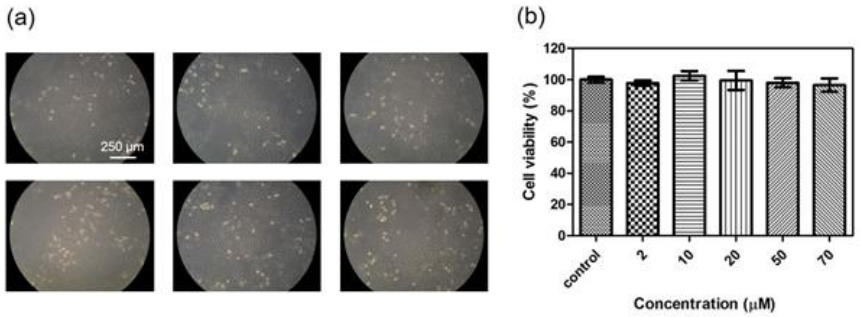

Figure S6. (a) Microscopic images of HeLa cells treated with 0, 2, 10, 20, 50, and 70 μM of **1** for 24 hours. The scale bar: 250 μm. (b) The viability of HeLa cells estimated by trypan blue exclusion assay. Data are shown as mean ± standard deviation.

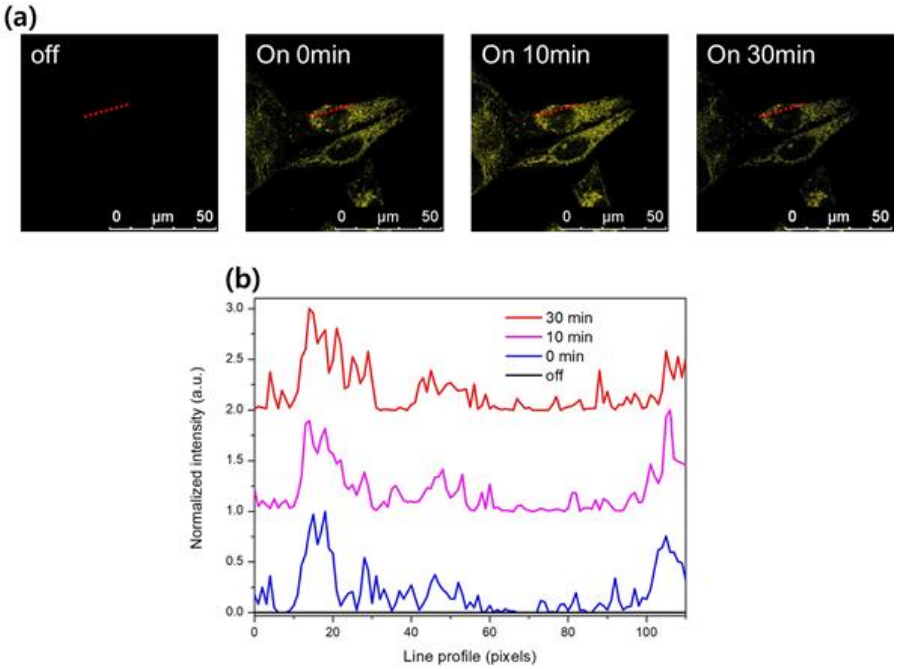

Figure S9. Line profiles of fluorescence intensity measured from HeLa cells. (a) Dashed red lines on HeLa cell images are shown for the intensity profile. (b) Normalized intensity line profiles measured by ImageJ 1.51.

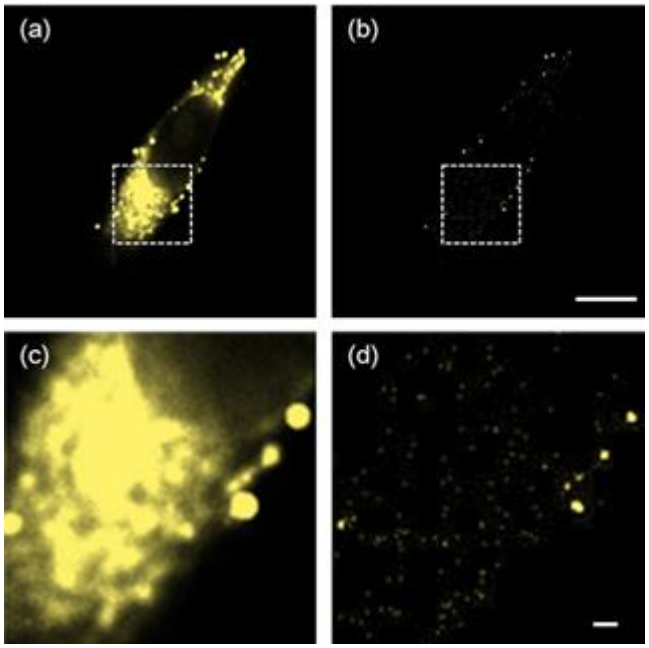

Figure 4. Super-resolution imaging experiments performed on HeLa cell. (a) A wide field image and (b) a super-resolution image of the whole imaging area. Scale bar: 10 μm. (c) A wide field image and (d) a super-resolution image of magnified area (the white square regions in (a) and (b), respectively). Scale bar: 1 μm

irradiation in the aqueous solution at pH between 3 and 10. It should be noted that its excellent photoswitching capability over broad pH range was maintained in the HeLa cells with low cytotoxicity. We also demonstrated its potential applicability for super-resolution imaging in cells by using PALM technique. We envision that the two sulfonate anion groups of **1** are able to interact with biological molecules and it would enable us to monitor some biological structures and dynamics even in harsh environments for further work.

3.5 Reference

1. Hell, S. W. *Science* **2007,** *316*, 1153-1158.

2. Hell, S. W. *Nat. Methods* **2009,** *6*, 24-32.

3. Dempsey, G. T.; Vaughan, J. C.; Chen, K. H.; Bates, M.; Zhuang, X. W. *Nat. Methods* **2011,** *8*, 1027-1036.

4. Fürstenberg, A.; Heilemann, M. *Phys. Chem. Chem. Phys.* **2013,** *15*, 14919-14930.

5. Heilemann, M.; Dedecker, P.; Hofkens, J.; Sauer, M. *Laser Photon. Rev.* **2009,** *3*, 180-202.

6. Zhou, J.; Yu, G.; Huang, F. *J. Mater. Chem. B* **2016,** *4*, 7761-7765.

7. Fernández-Suárez, M.; Ting, A. Y. *Rev. Mol. Cell Biol.* **2008,** *9*, 929-943.

8. Heilemann, M.; van de Linde, S.; Mukherjee, A.; Sauer, M. *Angew. Chem. Int. Ed.* **2009,** *48*, 6903-6908.

9. Fare, T. L.; Coffey, E. M.; Dai, H.; He, Y. D.; Kessler, D. A.; Kilian, K. A.; Koch, J. E.; LeProust, E.; Marton, M. J.; Meyer, M. R. *Anal. Chem.* **2003,** *75*, 4672-4675.

10. Cheng, H. B.; Hu, G. F.; Zhang, Z. H.; Gao, L.; Gao, X. F.; Wu, H. C. *Inorg Chem* **2016,** *55*, 7962-7968.

11. Kim, Y.; Jung, H. y.; Choe, Y. H.; Lee, C.; Ko, S. K.; Koun, S.; Choi, Y.; Chung, B. H.; Park, B. C.; Huh, T. L. *Angew. Chem. Int. Ed.* **2012,** *51*, 2878-2882.

12. Zou, Y.; Yi, T.; Xiao, S. Z.; Li, F. Y.; Li, C. Y.; Gao, X.; Wu, J. C.; Yu, M. X.; Huang, C. H. *J. Am. Chem. Soc.* **2008,** *130*, 15750-15751.

13. Li, C.; Gong, W.-L.; Hu, Z.; Aldred, M. P.; Zhang, G.-F.; Chen, T.; Huang, Z.-L.; Zhu, M.-Q. *RSC Adv.* **2013,** *3*, 8967-8972.

14. Li, C.; Hu, Z.; Aldred, M. P.; Zhao, L.-X.; Yan, H.; Zhang, G.-F.; Huang, Z.-L.; Li, A. D.; Zhu, M.-Q. *Macromolecules* **2014,** *47*, 8594-8601.

15. Nevskyi, O.; Sysoiev, D.; Oppermann, A.; Huhn, T.; Woll, D. *Angew. Chem. Int. Ed.* **2016,** *55*, 12698-12702.

16. Arai, Y.; Ito, S.; Fujita, H.; Yoneda, Y.; Kaji, T.; Takei, S.; Kashihara, R.; Morimoto, M.; Irie, M.; Miyasaka, H. *Chem. Commun.* **2017,** *53*, 4066-4069.

17. Roubinet, B.; Bossi, M. L.; Alt, P.; Leutenegger, M.; Shojaei, H.; Schnorrenberg, S.; Nizamov, S.; Irie, M.; Belov, V. N.; Hell, S. W. *Angew. Chem. Int. Ed.* **2016,** *55*, 15429-15433.

18. Guthrie, J. P. *Can. J. Chem.* **1978,** *56*, 2342-2354.

19. Krulwich, T. A.; Sachs, G.; Padan, E. *Nature Rev. Microbiol.* **2011,** *9*, 330-343.

20. Xu, Y.; Jiang, Z.; Xiao, Y.; Bi, F. Z.; Miao, J. Y.; Zhao, B. X. *Anal. Chim. Acta* **2014,** *820*, 146-151.

21. Yang, M.; Song, Y.; Zhang, M.; Lin, S.; Hao, Z.; Liang, Y.; Zhang, D.; Chen, P. R. *Angew. Chem. Int. Ed.* **2012,** *51*, 7674-7679.

22. Takagi, Y.; Morimoto, M.; Kashihara, R.; Fujinami, S.; Ito, S.; Miyasaka, H.; Irie, M. *Tetrahedron* **2017,** *73*, 4918-4924.

23. Um, S. H. M.S. Thesis, Seoul National University, Seoul, 2017.

24. Roubinet, B. t.; Weber, M.; Shojaei, H.; Bates, M.; Bossi, M. L.; Belov, V.

N.; Irie, M.; Hell, S. W. *J. Am. Chem. Soc.* **2017,** *139*, 6611-6620.

25. Yang, I.; Lee, J. W.; Hwang, S.; Lee, J. E.; Lim, E.; Lee, J.; Hwang, D.; Kim, C. H.; Keum, Y. S.; Kim, S. K. *J. Photochem. Photobiol. B, Biol.* **2017,** *166*, 52-57.

26. Halabi, E. A.; Thiel, Z.; Trapp, N.; Pinotsi, D.; Rivera-Fuentes, P. *J. Am. Chem. Soc.* **2017,** *139*, 13200-13207.

Appendix. Morphological analysis of oligomeric vs. fibrillar forms of α-synuclein aggregates with super-resolution BALM imaging

[This chapter was published in Chemical Physics Letters, 690, 62-67 (2017).]

A.1 Introduction

Recent advances in super-resolution optical nanoscopy enabled by methods such as STED and PALM/STORM have allowed *in situ* or *in vivo* analysis of subcellular structures with the unique advantages of lower sample damage and higher imaging contrast when compared to electron microscopy [1-9]. In particular, beyond a limited role as a conventional multi-color fluorescence imaging method, optical nanoscopy can lead to a quantitative co-localization analysis of membrane proteins, a pharmacological detection scheme by counting intracellular protein clusters, and a sub-structural mapping analysis for active sites of a single catalytic nanoparticle [10-13]. As these methods generally employ fluorescence detection, they often allow specific sample targeting as well. Among the protein fluorescence labelling methods, immuno-staining is widely used, but it tends to be costly and also limits the spatial resolution due to the considerable size of the antibody proteins themselves [14-18]. In this paper, we demonstrate the feasibility of staining dye-based super-resolution BALM (binding activated localization microscopy) imaging that does not rely on antibody labelling, but still targets a specific class of molecules; in this case, the aggregates of amyloid protein for sub-100 nm structural analysis.

More than 20 species of amyloid proteins have been discovered in the human body thus far, and most of them are associated with the pathogenesis of neurodegenerative diseases [19, 20]. Amyloid proteins are known to undergo aggregation through their hydrophobic interaction, which is believed to be ultimately linked to neuronal cell death [21, 22]. Studies found that of all forms of amyloid aggregates, the small, soluble

oligomeric form is most toxic and damaging to the neuronal system [23-28]. In clinical studies, some of these oligomeric proteins are tested as a candidate of early-stage biomarker for neurodegenerative disorders such as Parkinson's and Alzheimer's diseases [24]. Thus, the analytical ability for a diffraction-limited structure of amyloid aggregates is a key factor in developing an early-stage diagnostic tool for the disease.

Under *in vitro* or *in vacuo* conditions, morphological features of amyloid aggregates have been extensively studied by atomic force microscopy (AFM) [29], transmission electron microscopy (TEM) [30], and ion-drift mass spectrometry [31]. In contrast, optical imaging has only recently been attempted at the sub-diffraction level [18, 32, 33]. In 2011, Schierle *et al.* carried out *in situ* imaging of amyloid fibrils by dSTORM using immuno-staining to obtain a lateral resolution of 47 nm [18], which exceeds in size the thickness of the fibrils themselves (< 10 nm) due to the size of the antibody used in immuno-staining. In the present study, we adopted the BALM (binding activated localization microscopy) technique and implemented it with small-molecule staining dyes to overcome the resolution limit of immuno-staining.

BALM allows super-resolution nanoscopy using the localization and reconstruction of individual fluorophores as in STORM or PALM, but is not based on photoswitching. Instead, stochastic binding and unbinding of dyes with the target (Figure. 1) lead to an "on" state (bound) with a ~100-fold increase in fluorescence intensity or "off" state (unbound or photobleached). BALM was originally applied to image double-stranded DNA (dsDNA) *in vitro* or *in situ* using certain dyes (YOYO-1 and picogreen) and proper redox agents, and yielded structural images of dsDNA with a FWHM (full width at half maximum) of 9.8 nm [34]. It has

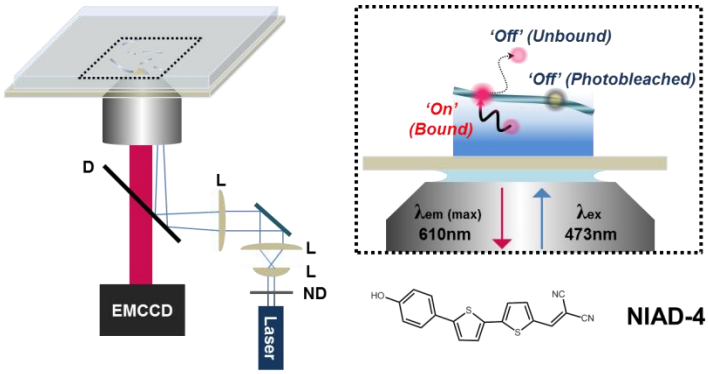

Figure 1. Schematic diagram of the sample chamber and optical configuration (D: Dichroic mirror, L: Lens, ND: Neutral density filter). The fibril-binding dye can be in an "on" state when bound to the fibril or "off" state when unbound or photobleached

been also useful in analyzing chromatin nano-architecture based on DNA structure fluctuations [35].

Recently, although no detailed morphological analysis was undertaken for heterogeneous aggregates of an amyloid, Ries et al. successfully applied super-resolution BALM imaging to amyloid fibrils [36]. In this paper, we demonstrate that BALM imaging can not only identify the distinct oligomeric *vs.* fibrillar structures of amyloid aggregates but also reveal sub-structural features of amyloid fibril. We also found that our BALM imaging with several mM of glutathione, which is comparable to the cytosolic condition, exhibits better photostability and efficiency of spatial resolution than with the commonly used imaging agent.

A.2 Experimental Method

A.2.1 Materials

In our experiments, fibril-binding dyes are allowed to be adsorbed on the surface of fibrils, which leads to a drastic increase in their fluorescence intensity compared to the intensity of a freely diffusing dye. For the staining dye, we mainly adopted NIAD-4 (Figure. 1) [37], a fibril-binding dye with a molecular weight of 334 Da and high permeability through the blood-brain barrier (BBB) to enable fluorescence imaging of amyloid aggregates in the brain. NIAD-4 also has high binding affinity with a small dissociation constant (K_d = 10 nM), which means that it is much more strongly binding than other common staining dyes such as thioflavin T (K_d = 580 nM) or Congo Red (K_d = 1,000 nM). A high binding affinity means that fluorescence imaging is feasible even with a minimal amount of dye (on the order of sub-nM scale).

Our sample was prepared in a dye solution after incubating the amyloid aggregates at room temperature for several minutes in the sample chamber. We synthesized NIAD-4 according to the procedures provided in literature [37]. After purifying the end product, we verified that the compound clearly matched the known structure of NIAD-4 through ^{1}H NMR (Figure. S1).

The amyloid aggregates were prepared by incubating α-synuclein (1 mg/mL) in PBS (20 mM, pH 7.0) while shaking at 250 rpm. A 20 μL aliquot of the aggregates was mixed with a 20 μL imaging buffer solution (PBS with a primary thiol such as mercaptoethyl amine (MEA), β-mercaptoethanol (BME), glutathione (GSH) or a scavenging system). The mixed sample was then injected into the sample chamber constructed by attaching a coverslip to a slide glass with double-sided tape as a spacer. After incubating for spontaneous adsorption on the poly-L-lysine coated coverslip, the fibril-binding dye solution (0.1 ~ 1,000 nM in imaging buffer) was injected into the chamber and incubated at room temperature for several minutes.

A.2.1 Microscope

BALM imaging was carried out using a customized total internal reflection fluorescence microscope based on a commercial inverted microscope (Olympus, IX71). Excitation lasers at 405 nm (Cube 405-100C, Coherent) and 473 nm (Blues TM50, Cobolt) were combined by a proper dichroic mirror (zt405rdc, Chroma). To illuminate the entire imaging area (36 μm x 36 μm), laser beams were expanded 12 times by a pair of tube lenses (LA1256-A, f = 300 mm and LA1951-A, f = 25 mm, Thorlabs) and converged by another lens (LAO-300.0-50.0/075, f =

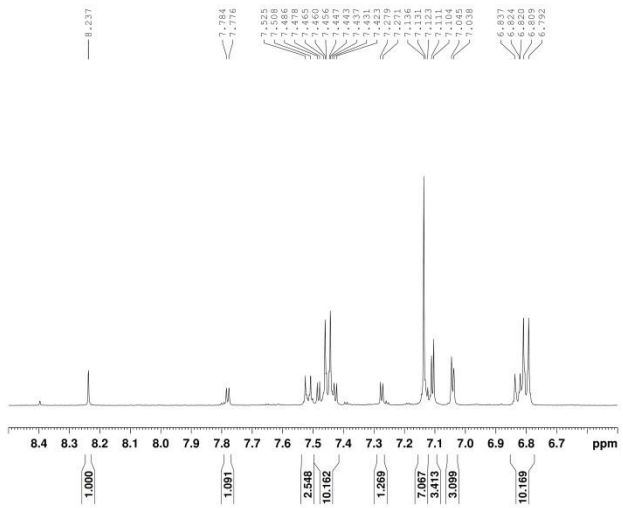

Figure S1. ^{1}H NMR spectrum of NIAD-4 in MeOD

300 mm, Melles-Griot) and an objective lens pair (UPLSAPO100XO, Olympus). The output power of the excitation laser was typically several milliwatts but we controlled the range from 3 to 30 mW for power dependency test. The total internal reflection was achieved by translating the illumination laser. The collected fluorescence was expanded by a pair of tube lenses (LAO-120.0-40.0/075, f = 120 mm and LAO-260.1-50.0/075, f = 260 mm, Melles-Griot) and imaged by an electron multiplying charged coupled device camera (EM-CCD, Andor, Ixon3). The camera exposure time was usually kept at 50 ms and ~20,000 frames of image were acquired for a single-BALM image.

A.2.3 Imaging analysis

Only pixels with photon counts greater than a threshold value were selected for image fitting. 7 x 7 pixels around a local maximum were fitted to a 2-D elliptical Gaussian function, and images that were too dim, too elliptic, too small, or too large were discarded. Bright spots that were detected in sequential frames within 1 pixel were regarded as coming from the same molecule and fitted after summing all the frames. To render a super-resolution or diffraction-limited fluorescence image, each localization result was represented as a Gaussian function with either 11-nm or 150-nm standard deviation, respectively. The unit pixel size was 5 nm for super-resolution image and 50 nm for diffraction-limited image. While checking the sample position in image data, we applied a lateral drift correction (Figure. S2) using an image cross-correlation method [38] every 50 frames.

The cross-sectional profile of amyloid fibrils was generated by collecting the number of localization spots along the cross-sectional line

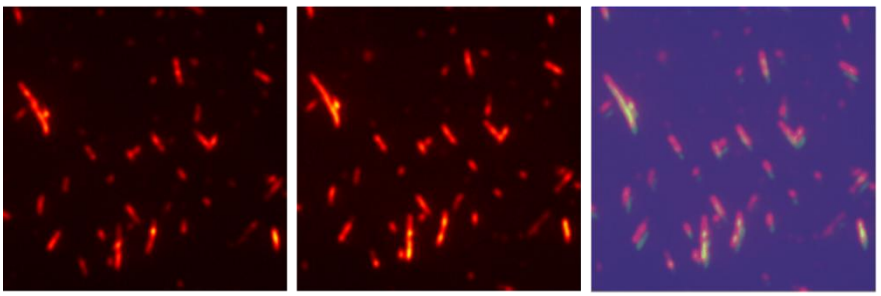

Figure S2. 50-frame averaged images of fibrils obtained to test lateral drift correction. The first 50-frame averaged image (left) and the last 50-frame averaged image (middle) show clear fibril morphology, indicating reliable drift correction at work. An overlap of these two images (right) shows that the lateral drift is marginal.

perpendicular to the long axis of the fibril over a specific length (300 nm). All analysis steps were carried out by using a home-built program written in MATLAB (MathWorks). The theoretical localization error (standard deviation of Gaussian distribution) was estimated using the following equation [39]:

$$\sigma = \sqrt{(s^2 + a^2/12)/N + 8\pi s^4 b^2/a^2 N^2}$$

, where N is the number of photons, s is the standard deviation of the point spread function, a is the pixel size, and b is the background noise. We used values of N and s averaged over several hundred thousand molecules in each BALM image. The value of b was estimated from the standard deviation of photon intensity in the region where no fluorophores were visible. A theoretical resolution was taken as the FWHM of the Gaussian distribution, i.e., ~2.35 times the standard deviation.

A.3 Results & Discussion

Figure 2 shows the BALM images of the wild type (WT) α-synuclein fibrils. Comparison of the diffraction-limited (Figure. 2A) vs. BALM (Figure. 2B) images shows that the latter offers a greatly improved spatial resolution as in the latest BALM imaging [36], with a FWHM fibril diameter of ~14 nm (Figure. 2C), which is at least two times smaller than that obtained previously by methods such as dSTORM using immuno-staining [18] and other localization microscopy [32, 33]. In localization-based super-resolution microscopy, the number of photons emitted from a single fluorophore is crucial since it is directly related to the localization precision and resolution of the final image. The red bars

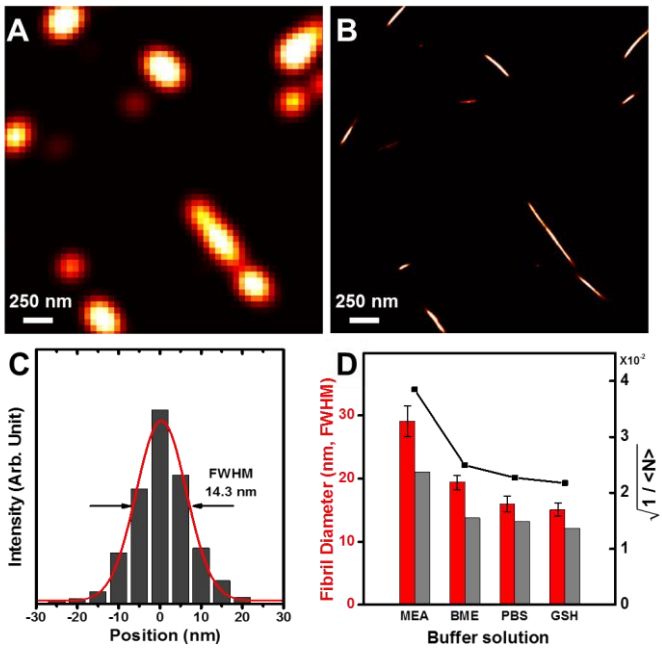

Figure 2. Optical images for the amyloid fibrils of WT α-synuclein obtained by (A) diffraction-limited and (B) BALM imaging with the staining dye NIAD-4. (C) The cross-sectional intensity across a fibril accumulated over a given length (300 nm) gives a Gaussian distribution, yielding a fibril diameter of ~14 nm FWHM. (D) Average fibril diameter (red bars; error bars showing the standard deviation for three arbitrarily chosen fibrils) measured by BALM using primary thiols MEA (mercaptoethyl amine), BME (β-mercaptoethanol), or GSH (glutathione) in PBS buffer, in comparison with pure PBS solution. The black squares represent 1/(average number of photons emitted)$^{1/2}$, which determines the spatial resolution in localization-based microscopy and are shown to scale well with our measured fibril diameters (red bars) as well as theoretically estimated spatial resolution (gray bars).

in Figure 2D represent the fibril diameters measured by BALM while the black dots indicate $1/\langle N \rangle^{1/2}$, which determines the spatial resolution in localization-based microscopy ($\langle N \rangle$ itself being given in Figure S4). We note that both quantities scale very well with the theoretically estimated spatial resolution (gray bars).

In previous studies, primary thiols were usually used to obtain better super-resolution images by enhancing the brightness of fluorophores and changing the kinetics of binding or switching [40-42]. We tested the performance of BALM imaging with three primary thiols (MEA, BME, and GSH) in PBS buffer along with pure PBS solution. In steady-state fluorescence, we found that GSH enhances the fluorescence from NIAD-4 most strongly among all buffers (Figure. S3). To check the relative performance of BALM imaging, after injecting the dye solution containing one of the above thiols into the sample chamber, we measured the average number of photons emitted from the fluorophore and the diameter of fibrils. We consistently observed that the tendency shown in Figure. S4 is similar to that of the steady-state spectrum shown in Figure. S3.

Speculating whether primary thiols affect the photostability of NIAD-4, we analyze the fluorescence signals in the equivalent conditions of BALM imaging including their time-averaged intensity and the rate of the photoswitching process. To measure the rate of the photoswitching process, we determined the efficient spot number by counting the number of efficiently fitted localization spots in the entire imaging area and averaging it over the observation time. In principle, a high level of the mean fluorescence intensity goes with high photostability whereas the rate of photoswitching tends to be anti-correlated with the stability

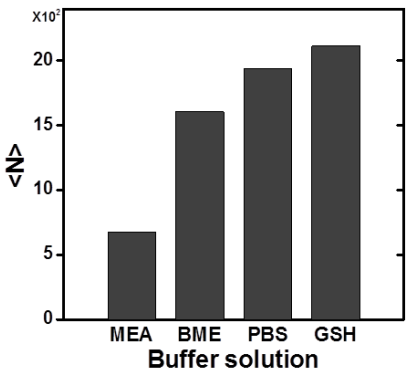

Figure S4. Average number of photons (<N>) emitted from a fluophore in primary thiols MEA (mercaptoethyl amine), BME (β-mercaptoethanol), or GSH (glutathione) in PBS buffer, when compared to pure PBS solution.

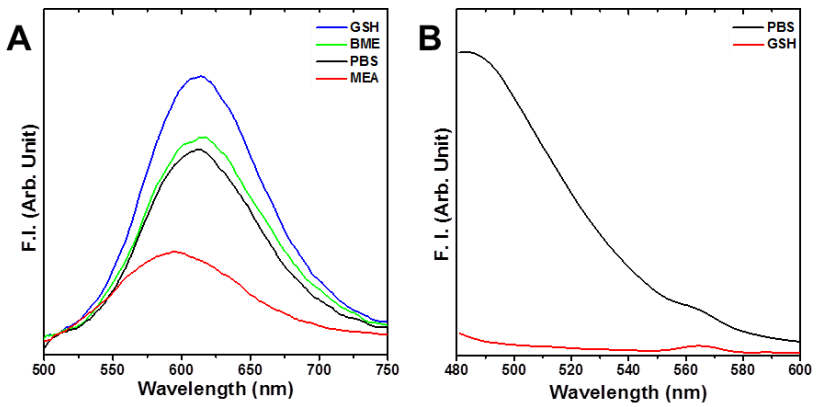

Figure S3. Fluorescence spectra of staining dyes, (A) NIAD-4 (with excitation at473 nm) and (B) Thioflavin T (with excitation at473 nm) with mature fibrils in PBS buffer condition (MEA, BME and GSH are mercaptoethyl amine, mercaptoethanol, and glutathione, respectively).

of the fluorophore. Considering the previous study that showed a triplet quencher (trolox, TRX) with an oxygen scavenging system [41, 43] imparted photostability to the fluorophore, it is reasonable that there is an anti-correlation between the mean intensity and the efficient spot number, except for the case of GSH (Figure. 3B). We assume that the role of GSH may be mainly as a reducing agent. The reducing property is related to the quenching process of the non-fluorescent dark state in the simplified diagram (process 2 in Figure. 3C). By testing the power dependency (Figure. 3D), the efficient spot number for the GSH case shows a large power dependence due to the photobleaching process. We conclude that GSH is an efficient reducing agent that prevents the photo-bleaching process of NIAD-4 to make BALM imaging amenable for in situ or in vivo assay under the physiological condition.

For the polymorphism of the amyloid fibrils, as resolved by TEM and AFM measurements [29, 30], we simply applied BALM to the ribbon-like morphological image of the amyloid fibrils. To compare the periodicity of the fibrils with previous results, we investigated the interval of the local maximum points in the intensity profile across the axis of the fibrils, which found that the average periodic interval of 44 ±3 nm (Figure. S5) is in good agreement with the twisted ribbon-like structure with an interval of 46 nm, as found previously from AFM measurements [44-46]. In contrast to the mature amyloid fibrils shown in Figure. 4A, we attempted to distinguish morphologically distinctive features of the oligomeric form of amyloid aggregates that consist of several tens of monomer units [47, 48]. In order to obtain a sufficient number of oligomers, we applied a disaggregation method to mature fibrils by incubating them at a temperature below −15 ℃ in what is known as cold-induced

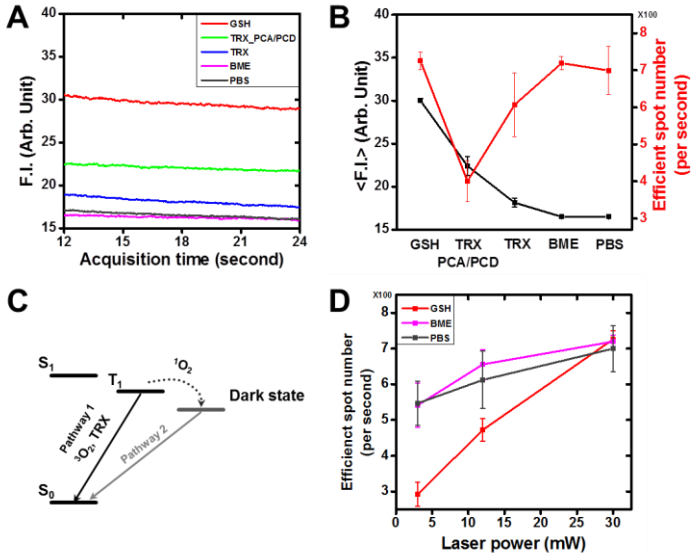

Figure 3. (A) Fluorescence intensity plot of fluorophore (NIAD-4) on fibrils over the imaging area (36 μm x 36 μm) shows that the intensity varies dramatically with the imaging condition and the fluorophores. (TRX: Trolox, PCA/PCD: enzymatic oxygen scavenging system) (B) Averaged fluorescence intensity (black squares) vs. efficient spot number (red squares) shows that they are mainly anti-correlated, except for the case of GSH. (C) A simplified Jablonski diagram of the organic fluorophore. In general, the photoswitching process occurs through a triplet state (T_1) leading to the photo-blinking pathway 1 and a dark state leading to the photo-blinking pathway 2. (D) The power dependency of the efficient spot number over the excitation laser power (3, 12, 30 mW)

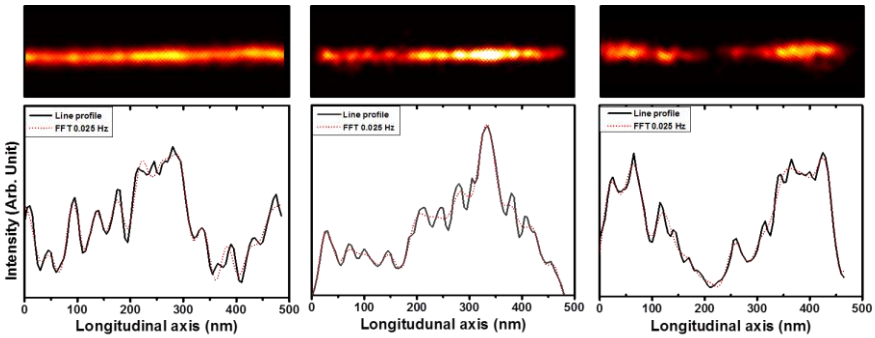

Figure S5. The fibrils produced from mutant protein E46K reveal a periodic intensity, which is consistent with the twisted ribbon-like substructure found by AFM. As shown in a cross-sectional view of the fibril under the BALM images, the interval analysis over a few fibrils has a characteristic periodicity of a twisted fibril. Through an FFT analysis by the Origin 8.5 software with their line profile, the periodic interval is determined to be around 40 nm, which is in good agreement with previous AFM results

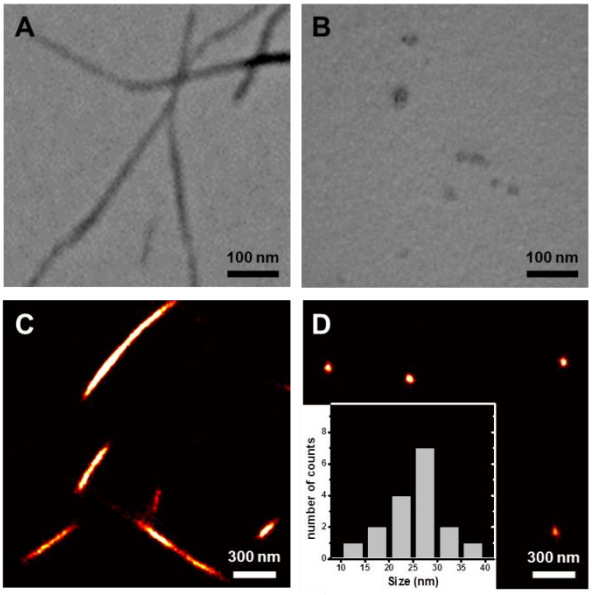

Figure 4. TEM image of (A) mature amyloid fibrils and (B) oligomers from disaggregation of mature amyloid fibrils by cold-induced dissociation, which are stained with 1% ammonium molybdate at pH 7.0. The BALM images of aggregates in (C) correspond to the fibrils in (A) and the image in (D) correspond to disaggregated oligomers in (B). As shown in (D), the size distribution of the round objects (inset, left) detected by BALM imaging shows an average diameter of 26 nm.

dissociation [49]. As shown in the TEM data (Figure. 4B), the fibrils are disaggregated into distinct round shapes with diameters of several tens of nm, which are consistent with the morphological features of amyloid oligomers observed in previous TEM and AFM results [49]. Within our lateral resolution (the average number of photons emitted, <N>, being around 2,000 and comparable to that of fibrils shown in Figure. 4C), we found a number of oligomers from the same disaggregation sample (Figure. 4D), which were remarkably similar in size and shape to those in the TEM image. The size distribution of these oligomers as detected by BALM imaging ranges from 10 to 40 nm in diameter (inset of Figure. 4D, left panel), again in accord with the results of the previous TEM analysis.

A.4 Conclusion

We applied the recently developed BALM technique to imaging amyloid aggregates using the staining dye NIAD-4. Super-resolution images were obtained for amyloid aggregates without immuno-staining, which delivered highly resolved optical images of amyloid fibrils with a FWHM of ~14 nm. The super-resolution capability of BALM revealed a substructure of mutant-derived fibrils consistent with a twisted ribbon-like structure found previously by AFM. It also appears that we may have been able to optically image amyloid oligomers, the most toxic form of amyloid aggregates, which greatly enhances the prospect of addressing amyloid-related diseases in diagnosis and drug tests by allowing facile *in situ* and *in vivo* detection by optical imaging.

A.5 Reference

1. S.W. Hell, J. Wichmann, Breaking the Diffraction Resolution Limit by Stimulated-Emission: Stimulated-Emission-Depletion Fluorescence Microscopy, Opt Lett 19 (1994) 780-782.

2. S.W. Hell, Far-field optical nanoscopy, Science 316 (2007) 1153-1158.

3. E. Betzig, G.H. Patterson, R. Sougrat, O.W. Lindwasser, S. Olenych, J.S. Bonifacino, M.W. Davidson, J. Lippincott-Schwartz, H.F. Hess, Imaging intracellular fluorescent proteins at nanometer resolution, Science 313 (2006) 1642-1645.

4. M.J. Rust, M. Bates, X.W. Zhuang, Sub-diffraction-limit imaging by stochastic optical reconstruction microscopy (STORM), Nat Methods 3 (2006) 793-795.

5. S.T. Hess, T.P.K. Girirajan, M.D. Mason, Ultra-high resolution imaging by fluorescence photoactivation localization microscopy, Biophys J 91 (2006) 4258-4272.

6. B. Huang, M. Bates, X.W. Zhuang, Super-Resolution Fluorescence Microscopy, Annu Rev Biochem 78 (2009) 993-1016.

7. S. van de Linde, M. Heilemann, M. Sauer, Live-Cell Super-Resolution Imaging with Synthetic Fluorophores, Annu Rev Phys Chem 63 (2012) 519-540.

8. R.S. Fischer, Y.C. Wu, P. Kanchanawong, H. Shroff, C.M. Waterman, Microscopy in 3D: a biologist's toolbox, Trends Cell Biol 21 (2011) 682-691.

9. S.W. Hell, S.J. Sahl, M. Bates, X.W. Zhuang, R. Heintzmann, M.J. Booth, J. Bewersdorf, G. Shtengel, H. Hess, P. Tinnefeld, A. Honigmann, S. Jakobs, I. Testa, L. Cognet, B. Lounis, H. Ewers, S.J. Davis, C. Eggeling, D. Klenerman, K.I. Willig, G. Vicidomini, M. Castello, A. Diaspro, T. Cordes, The 2015 super-resolution microscopy roadmap, J Phys D Appl Phys 48 (2015) 443001.

10. H. Deschout, A. Shivanandan, P. Annibale, M. Scarselli, A. Radenovic,

Progress in quantitative single-molecule localization microscopy, Histochem Cell Biol 142 (2014) 5-17.

11. P. Winckler, L. Lartigue, G. Giannone, F. De Giorgi, F. Ichas, J.B. Sibarita, B. Lounis, L. Cognet, Identification and super-resolution imaging of ligand-activated receptor dimers in live cells, Sci Rep-Uk 3 (2013) 2387.

12. Z. Truan, L. Tarancon Diez, C. Bonsch, S. Malkusch, U. Endesfelder, M. Munteanu, O. Hartley, M. Heilemann, A. Furstenberg, Quantitative morphological analysis of arrestin2 clustering upon G protein-coupled receptor stimulation by super-resolution microscopy, J Struct Biol 184 (2013) 329-334.

13. J.B. Sambur, T.Y. Chen, E. Choudhary, G.Q. Chen, E.J. Nissen, E.M. Thomas, N.M. Zou, P. Chen, Sub-particle reaction and photocurrent mapping to optimize catalyst-modified photoanodes, Nature 530 (2016) 77-80.

14. G. Patterson, M. Davidson, S. Manley, J. Lippincott-Schwartz, Superresolution Imaging using Single-Molecule Localization, Annual Review of Physical Chemistry, Vol 61 61 (2010) 345-367.

15. J.C. Vaughan, S. Jia, X.W. Zhuang, Ultrabright photoactivatable fluorophores created by reductive caging, Nat Methods 9 (2012) 1181-1184.

16. J. Ries, C. Kaplan, E. Platonova, H. Eghlidi, H. Ewers, A simple, versatile method for GFP-based super-resolution microscopy via nanobodies, Nat Methods 9 (2012) 582-584.

17 F. Opazo, M. Levy, M. Byrom, C. Schafer, C. Geisler, T.W. Groemer, A.D. Ellington, S.O. Rizzoli, Aptamers as potential tools for super-resolution microscopy, Nat Methods 9 (2012) 938-939.

18. G.S.K. Schierle, S. van de Linde, M. Erdelyi, E.K. Esbjorner, T. Klein, E. Rees, C.W. Bertoncini, C.M. Dobson, M. Sauer, C.F. Kaminski, In Situ Measurements of the Formation and Morphology of Intracellular beta-

Amyloid Fibrils by Super-Resolution Fluorescence Imaging, J Am Chem Soc 133 (2011) 12902-12905.

19 B. Caughey, P.T. Lansbury, Protofibrils, pores, fibrils, and neurodegeneration: Separating the responsible protein aggregates from the innocent bystanders, Annu Rev Neurosci 26 (2003) 267-298.

20 J.D. Sipe, Amyloid Proteins: The Beta Sheet Conformation and Disease, WILEY-VCH Verlag GmbH & Co. KGaA (2005).

21. J.W. Kelly, W.E. Balch, The integration of cell and chemical biology in protein folding, Nat Chem Biol 2 (2006) 224-227.

22. D.J. Selkoe, Normal and Abnormal Biology of the Beta-Amyloid Precursor Protein, Annu Rev Neurosci 17 (1994) 489-517.

23. T.T. Ding, S.J. Lee, J.C. Rochet, P.T. Lansbury, Annular alpha-synuclein protofibrils are produced when spherical protofibrils are incubated in solution or bound to brain-derived membranes, Biochemistry-Us 41 (2002) 10209-10217.

24. D.J. Selkoe, Biochemistry and Molecular Biology of Amyloid β-Protein and the Mechanism of Alzheimer's Disease, Handbook of Clinical Neurology, Elsevier2008, pp. 245-260.

25. I.F. Tsigelny, Y. Sharikov, W. Wrasidlo, T. Gonzalez, P.A. Desplats, L. Crews, B. Spencer, E. Masliah, Role of α-synuclein penetration into the membrane in the mechanisms of oligomer pore formation, The FEBS journal 279 (2012) 1000-1013.

26. J. Lee, E.K. Culyba, E.T. Powers, J.W. Kelly, Amyloid-beta forms fibrils by nucleated conformational conversion of oligomers, Nat Chem Biol 7 (2011) 602-609.

27. R. Kayed, E. Head, J.L. Thompson, T.M. McIntire, S.C. Milton, C.W. Cotman, C.G. Glabe, Common structure of soluble amyloid oligomers implies

common mechanism of pathogenesis, Science 300 (2003) 486-489.
28. M.J. Volles, P.T. Lansbury, Zeroing in on the pathogenic form of alpha-synuclein and its mechanism of neurotoxicity in Parkinson's disease, Biochemistry-Us 42 (2003) 7871-7878.
29. J. Adamcik, J.M. Jung, J. Flakowski, P. De Los Rios, G. Dietler, R. Mezzenga, Understanding amyloid aggregation by statistical analysis of atomic force microscopy images, Nat Nanotechnol 5 (2010) 423-428.
30. M. Fändrich, J. Meinhardt, N. Grigorieff, Structural Polymorphism of Alzheimer Aβ and Other Amyloid Fibrils, Prion 3 (2009) 89-93.
31. D.B. Teplow, N.D. Lazo, G. Bitan, S. Bernstein, T. Wyttenbach, M.T. Bowers, A. Baumketner, J.E. Shea, B. Urbanc, L. Cruz, J. Borreguero, H.E. Stanley, Elucidating amyloid beta-protein folding and assembly: A multidisciplinary approach, Accounts Chem Res 39 (2006) 635-645.
32. W.C. Duim, B. Chen, J. Frydman, W.E. Moerner, Sub-Diffraction Imaging of Huntingtin Protein Aggregates by Fluorescence Blink-Microscopy and Atomic Force Microscopy, Chemphyschem 12 (2011) 2387-2390.
33. M.J. Roberti, J. Folling, M.S. Celej, M. Bossi, T.M. Jovin, E.A. Jares-Erijman, Imaging Nanometer-Sized alpha-Synuclein Aggregates by Superresolution Fluorescence Localization Microscopy, Biophys J 102 (2012) 1598-1607.
34. I. Schoen, J. Ries, E. Klotzsch, H. Ewers, V. Vogel, Binding-Activated Localization Microscopy of DNA Structures, Nano Lett 11 (2011) 4008-4011.
35. A. Szczurek, L. Klewes, J. Xing, A. Gourram, U. Birk, H. Knecht, J.W. Dobrucki, S. Mai, C. Cremer, Imaging chromatin nanostructure with binding-activated localization microscopy based on DNA structure fluctuations, Nucleic Acids Res (2017) 1-11.
36. J. Ries, V. Udayar, A. Soragni, S. Hornemann, K.P.R. Nilsson, R. Riek, C.

Hock, H. Ewers, A.A. Aguzzi, L. Rajendran, Superresolution Imaging of Amyloid Fibrils with Binding-Activated Probes, Acs Chem Neurosci 4 (2013) 1057-1061.

37. E.E. Nesterov, J. Skoch, B.T. Hyman, W.E. Klunk, B.J. Bacskai, T.M. Swager, In vivo optical Imaging of amyloid aggregates in brain: Design of fluorescent markers, Angew Chem Int Edit 44 (2005) 5452-5456.

38. M. Guizar-Sicairos, S.T. Thurman, J.R. Fienup, Efficient subpixel image registration algorithms, Opt Lett 33 (2008) 156-158.

39. R.E. Thompson, D.R. Larson, W.W. Webb, Precise nanometer localization analysis for individual fluorescent probes, Biophys J 82 (2002) 2775-2783.

40. G.T. Dempsey, J.C. Vaughan, K.H. Chen, M. Bates, X.W. Zhuang, Evaluation of fluorophores for optimal performance in localization-based super-resolution imaging, Nat Methods 8 (2011) 1027-1036.

41. T. Ha, P. Tinnefeld, Photophysics of Fluorescent Probes for Single-Molecule Biophysics and Super-Resolution Imaging, Annu Rev Phys Chem 63 (2012) 595-617.

42. J. Vogelsang, C. Steinhauer, C. Forthmann, I.H. Stein, B. Person-Skegro, T. Cordes, P. Tinnefeld, Make them Blink: Probes for Super-Resolution Microscopy, Chemphyschem 11 (2010) 2475-2490.

43. M. Swoboda, J. Henig, H.M. Cheng, D. Brugger, D. Haltrich, N. Plumere, M. Schlierf, Enzymatic Oxygen Scavenging for Photostability without pH Drop in Single-Molecule Experiments, Acs Nano 6 (2012) 6364-6369.

44. J.S. Pedersen, C.B. Andersen, D.E. Otzen, Amyloid structure – one but not the same: the many levels of fibrillar polymorphism, FEBS Journal 277 (2010) 4591-4601.

45. A.T. Petkova, R.D. Leapman, Z.H. Guo, W.M. Yau, M.P. Mattson, R.

Tycko, Self-propagating, molecular-level polymorphism in Alzheimer's beta-amyloid fibrils, Science 307 (2005) 262-265.

46. K.K.M. Sweers, I.M.J. Segers-Nolten, M.L. Bennink, V. Subramaniam, Structural model for alpha-synuclein fibrils derived from high resolution imaging and nanomechanical studies using atomic force microscopy, Soft Matter 8 (2012) 7215-7222.

47. I. Benilova, E. Karran, B. De Strooper, The toxic A beta oligomer and Alzheimer's disease: an emperor in need of clothes, Nat Neurosci 15 (2012) 349-357.

48. N. Zijlstra, C. Blum, I.M.J. Segers-Nolten, M.M.A.E. Claessens, V. Subramaniam, Molecular Composition of Sub-stoichiometrically Labeled a-Synuclein Oligomers Determined by Single-Molecule Photobleaching, Angew Chem Int Edit 51 (2012) 8821-8824.

49. H.Y. Kim, M.K. Cho, A. Kumar, E. Maier, C. Siebenhaar, S. Becker, C.O. Fernandez, H.A. Lashuel, R. Benz, A. Lange, M. Zweckstetter, Structural Properties of Pore-Forming Oligomers of alpha-Synuclein, J Am Chem Soc 131 (2009) 17482-17489.

국문초록

분석 기술로 활용한 초고분해능 이미징 기술의 응용 연구

김 형 준

물리화학 전공

화학부

서울대학교

광학 형광 현미경은 세포 내에 존재하는 다양한 생분자를 선택적이고 높은 감도로 볼 수 있는 이미징 기술이다. 이 기술은 단순히 시공간에서 분포하는 물질의 구조뿐만 아니라 분자간의 상호관계 등 다양한 정보를 얻을 수 있기 때문에, 화학, 의학, 공학분야에서도 널리 사용되고 있다. 특히 초고분해능 광학 영상 기술은 광학 현미경의 회절한계를 뛰어넘어 다양한 물질의 구조를 분자수준에서 관찰할 수 있게 만들었고, 관련된 현상의 메커니즘 연구에 크게 기여할 수 있었다. 하지만 기술발전에도 불구하고, 이를 이용한 응용연구는 초창기 광학 나노스코피 개발자들에게만 대부분 국한돼있고, 응용연구사례 또한 적다. 따라서 본 연구에서는 광학 나노스코피 기술을 활용하고 발전시켜 유전자, 미토콘드리아, 단백질 등을 분석할 수 있는 방법을 개발하고자 하였다.

데옥시리보핵산(이하 유전자)는 유전 정보를 포함하고 있는 대표적인 고분자이다. 사람마다 가지고 있는 유전자 변이 차이는 신체구조와 같은 다양한 형질로 표현되기도 하고, 암, 당뇨병, 알츠하이머 등 여러 질병에서도 복잡하고 개별적인 유전자 변이를 갖는다. 그러므로 유전자 변이를 이해하고 생명 현상과의 관련성을 파악하는 것은 매우 중요한 문제이다. 유전자 변이중에도 최근 들어 유전자 복

제수 변이(이하 CNV)가 사람의 유전자에 광범위하게 존재한다고 알려지면서 많은 연구자들이 CNV 연구에 참여하고 있다. CNV 는 유전자의 특정 염기 서열의 길이가 증가하거나 결실되는 현상으로 수백 에서 수백만 염기쌍 범위에서 길이차이를 보인다. 하지만 유전자는 그 크기가 회절한계보다 작아서 유전자 발현과 같은 구조변화를 연구하는데 많은 한계가 따른다. 따라서 본 연구에서는 초고분해능의 스테드 기술로 제한 효소에 의해 잘려진 다양한 길이의 유전자를 정확히 측정함으로써, 초고분해능 광학 현미경을 유전자 복제수 변이 연구에 활용할 수 있는 가능성을 가늠하는 기반 연구를 진행하였다. BstE Ⅱ 와 Hind Ⅲ 제한 효소로 처리된 람다유전자조각을 공초점현미경 및 스테드 이미지로부터 길이를 측정하고 평균값을 구해 참고문헌의 값과 비교해 보았다. 측정한 모든 길이에서 스테드로 측정한 람다유전자조각들이 참고문헌의 값과 근사한 것을 확인하였다. 반면 공초점현미경 이미지로부터 얻은 람다유전자조각의 길이는 약 200-400 나노미터 정도의 길이오차를 보였다. BstE Ⅱ 제한효소로 처리된 람다유전자조각는 2323 염기쌍 이하(약 1.5 마이크로미터 이하)의 짧은 길이의 유전자조각이 다양하게 존재하였고, 약 100 염기쌍 길이 차이가 나는 유전자조각들도 정확하기 구분하는 것이 가능하였다.

세포 소기관 중 하나인 미토콘드리아는 세포의 에너지 대사 및 기능을 유지하는데 매우 중요한 역할을 한다. 더욱이 노화가 진행됨에 따라 미토콘드리아의 기능을 조절하는 주요 조절인자의 활성과 수가 감소하며, 이것이 미토콘드리아의 결핍을 가중시킨다. 따라서 본 연구에서는 형광을 기반으로 하는 초고분해능 광학 영상기술로 자외선을 이용한 노화유도 자극에 의해 변화된 미토콘드리아를 정량적으로 분석하여 노화의 정도를 판별할 수 있는 분석 기술을 확립하고자 한다. 먼저 사람의 피부로부터 분리된 섬유아세포를 계대배양하고 노화를 유도시키는 자극으로 알려진 자외선(UVB)에 노출시켜 세포손상을 유도하였다. 미토콘드리아의 전반적인 구조 변화 및 노화와 관련된 인자의 변화를 관찰하기 위해 미토콘드리아의 외막에 분포하는 TOM20 와 미토콘드리아 DNA 와 핵양체를 구성하고 있는 TFAM 항체를 이용해 표지하였고, 초고분해능 광학 영상 장치로 관찰하였다. 기존의 현미경 기술을 대변할 수 있는 공초점 현미경으로는 회절한계 이하에서 일어나는 변화를 영상적으로 구분할 수 없었으나, 초고분해능 영상 기술(STED)로 관찰한 이미지에서는 회절한계 이하에서 생기는 translocase 분포 변화와 핵양체의 정량적인 차이를 분석할 수 있었다. 나아가 만성적으로 노화가 유도된 쥐

의 피부 조직에서도 미토콘드리아의 변화를 관찰하였다. 따라서 초고분해능 형광 현미경을 이용한 미토콘드리아의 구조 변화 분석 기술을 발전 시키면 노화의 정도를 정량화 해 생체 연령 측정 기술로 활용할 수 있으리라 기대한다.

높은 수용성의 디아릴에텐 형광 분자를 합성하였고, 이 분자를 바이오 이미징에 활용할 수 있는지 가능성을 평가하고자 하였다. 술폰산염 작용기를 가진 디아릴에텐은 높은 수용성을 가지고 광범위한 pH 범위에서 응집 및 특성변화 없이 광변색이 가능한 것을 확인하였다. 또한 세포 내에서도 이 분자의 주요 특성이 유지되며, 독성도 낮은 것을 확인하였다. 마지막으로 초고분해능 광학 영상 현미경에서도 이 분자를 활용할 수 있는지 실험해 보았다.

아밀로이드 응집체에 대한 특이성을 가지는 형광분자를 도입한 초고분해능 형광 이미징 기술(이하 BALM)을 개발하였다. 응집체 흡착 특성을 가지는 형광분자는 아밀로이드 응집체 형광 과정을 관측하는데 유용하다. 본 연구에서는 밤 기술로 박테리아 내에서 일어난 아밀로이드 단백질의 응집과정을 관찰하였다. 대표적으로 알파 나선 구조를 가지는 수십 나노미터 크기의 올리고머 형태를 관찰하였고, 이 올리고머가 피브릴 변환 과정에서 이상 경로를 유도하는 물질임을 확인하였다. 따라서 밤 기술 개발은 아밀로이드 관련 질병을 연구하거나 신약개발을 하는데 있어서 유용한 도구로 활용될 수 있을 것으로 기대한다.

.....

주요어 : 스테드 나노스코피, 동적분자빗질, 데옥시리보핵산,
미토콘드리아, 광스위칭 형광체, 초고분해능 이미징.

학번 : 2011-30100